


Manifestations of local supersolidity of ^4He around a charged molecular impurity

Fabien Briec,^{*} Christoph Schran^{Ⓜ,†} and Dominik Marx[‡]

Lehrstuhl für Theoretische Chemie, Ruhr-Universität Bochum, 44780 Bochum, Germany

 (Received 20 January 2023; revised 21 July 2023; accepted 21 August 2023; published 26 October 2023)

A frozen, solid helium core, dubbed a snowball, is typically observed around cations in liquid helium. Here we discover, using path integral simulations, that around a cationic molecular impurity, protonated methane, the ^4He atoms are indeed strongly localized akin to snowballs but still participate in vivid bosonic exchange induced by the rovibrational motion of the impurity. Such a combination of solidlike order with pronounced superfluid response in the first helium shell indicates that manifestations of local supersolid behavior of ^4He can be induced by charged molecules.

DOI: [10.1103/PhysRevResearch.5.043083](https://doi.org/10.1103/PhysRevResearch.5.043083)

I. INTRODUCTION

Since the groundbreaking discovery of superfluidity in liquid ^4He , generations of scientists have raised the question whether such a superfluid response can persist in the solid phase, i.e., can a solid be superfluid? [1]. Such a counterintuitive state, combining solidlike order with a finite superfluid fraction [2], has been theoretically proposed as early as 1969 [3,4]. More recently, it has been suggested experimentally that supersolid states can appear in model systems, such as Bose-Einstein condensates of atomic gases at ultralow temperatures [5–7]. Computationally, evidence of a supersolid phase has been reported for atomic deuterium—yet at ultrahigh pressure conditions [8]. When it comes to finite systems, substantial understanding was provided by theoretical work leading to novel experiments. In fact, pioneering path integral simulations have revealed that small para- H_2 clusters of a specific size can exhibit spatial localization of these bosonic species at sufficiently low temperatures, reminiscent of a solid, combined with some remaining bosonic exchange [9,10], thus suggesting supersolid behavior. But different from para- H_2 , such phenomena cannot appear in pure ^4He clusters since they remain liquid even in the ground state given that the very weak $\text{He} \cdots \text{He}$ interactions are a factor of 3 smaller. Overall, the existence of supersolid properties in the specific case of ^4He systems, both extended and finite, remains controversial [2,11–14].

Here, we answer the question whether *manifestations of supersolid behavior* of ^4He can be found *locally* in the first shell around charged molecular impurities in finite ^4He systems—a situation that would potentially enable experimental verification akin to discovering *microscopic manifestation of superfluidity* around neutral dopant molecules [15–17].

Indeed, such impurities in liquid helium have been shown to be powerful probes of “*manifestations of superfluid behavior*,” a concept introduced by seminal theory work [18], and validated experimentally a decade later [15–17]. Charged impurities usually interact strongly with helium, creating a frozen, solidlike core around the impurity, referred to as a snowball [19]. This snowball effect has been extensively studied both theoretically [20–22] and experimentally [23–25] in the case of atomic cationic impurities, and has been linked to a local *disappearance of superfluidity* within the frozen ^4He atoms of the snowball due to their strong spatial localization [20,22,26].

Molecular impurities have also been immersed, particularly, in helium nanodroplets and smaller ^4He clusters [17]. Their rotational excitations have been used to probe the local microscopic superfluid response showing that manifestations of superfluid behavior can indeed be found in finite systems as small as about ten ^4He atoms only [27–29]. In addition, quantum simulations have been pivotal in elucidating the impact of neutral molecular impurities on the helium environment [30–34]. Their impact is usually smaller than ions due to weaker interactions with the solvent. However, around some of the most strongly interacting neutral molecules, such as SF_6 , the first solvation shell is composed of more localized ^4He atoms, which is linked to a *reduction* of the superfluid fraction in a way that is reminiscent of the snowball effect around ions [30,35]. Yet, it has been shown that rigid-body rotation can lead to a non-negligible *enhancement* of the superfluid response in the first shell [36–39]. Pioneering work on the superfluid response of ^4He around C_{20} has even hinted at something like nanoscale supersolidity but, akin to para- H_2 clusters, only for specific (magic) helium numbers between 28 and 31 atoms, whereas the phenomenon quickly vanishes when adding more ^4He atoms [40]. Similar effects have also been seen around the completion of the second layer of helium adsorbed on graphite [41–43].

^{*}Present address: Laboratoire Matière en Conditions Extrêmes, Université Paris-Saclay, CEA, 91680 Bruyères-le-Châtel; CEA, DAM, DIF, F-91297 Arpajon, France; fabien.briec@cea.fr

[†]Present address: Cavendish Laboratory, Department of Physics, University of Cambridge, Cambridge, CB3 0HE, United Kingdom; cs2121@cam.ac.uk

[‡]dominik.marx@rub.de

Published by the American Physical Society under the terms of the [Creative Commons Attribution 4.0 International license](https://creativecommons.org/licenses/by/4.0/). Further distribution of this work must maintain attribution to the author(s) and the published article's title, journal citation, and DOI.

In that longstanding quest of finding manifestations of supersolid behavior in ^4He , this leads to the question whether fast rotation of strongly interacting molecular impurities could induce a pronounced superfluid response in a frozen, solidlike helium shell, and thus could be used as seeds for supersolid behavior in the bulk.

To answer this fundamental question, we set out to study helium solvation of an ionic molecular impurity, protonated methane, using quantum simulations. Why CH_5^+ ? First, its interaction with ^4He is about four times stronger than other strongly interacting neutral species. Second, CH_5^+ is a prototype of the class of so-called fluxional molecules, being subject to large-amplitude motion leading to a full delocalization of its hydrogens due to pseudorotational motion [44]. The combination of these intramolecular pseudorotations with the standard rotations of the molecule leads to entangled $\text{SO}(5)$ “superrotational motion” [45]. This complex and rich hydrogen scrambling dynamics remains unperturbed under helium solvation [46] in agreement with our present findings. Third, an intricate coupling has recently been discovered between the complex rovibrational motion of CH_5^+ and bosonic exchange in the *microsolvation limit* with up to only four ^4He atoms [47].

We study quantum solvation and superfluid response of CH_5^+ in ^4He nanoclusters of up to 60 helium atoms and unveil a phenomenon that cannot appear in the microsolvation limit. These results are referenced to CH_4 in helium [39] to compare to this ordinary cousin of CH_5^+ . Contrary to CH_5^+ , CH_4 is a standard quasirigid molecule subject to small-amplitude motion that is well described by quasiharmonic deviations from a unique equilibrium structure. Moreover, as most neutral species, CH_4 does not feature such strong interactions as CH_5^+ with helium.

II. METHODS AND COMPUTATIONAL DETAILS

All simulations of CH_5^+ and CH_4 solvated in clusters composed of $n = 1$ up to 60 ^4He atoms have been carried out at $T = 0.5$ K using finite-temperature bosonic path integral techniques. This approach takes into account the full molecular flexibility at an essentially converged coupled cluster level as recently reviewed in Ref. [48]. Accordingly, we used a hybrid approach combining path integral molecular dynamics (PIMD) with path integral Monte Carlo (PIMC) [49] in which helium is sampled using PIMC [50] to account for the bosonic nature of ^4He , whereas the molecule is described using PIMD. More precisely, the configuration and permutation space of bosonic helium is sampled using the continuous-space worm algorithm [51,52] (in the specific canonical variant introduced in the Appendix of Ref. [48]), while the configuration space of the impurity is sampled using the path integral quantum thermal bath (PIQTB) technique [53] as adapted and validated for path integral simulations at very low temperatures [54]. Path integral convergence is achieved by describing the helium density matrix within the pair density approximation [50] using a high-temperature matrix computed at $T = 80$ K, resulting in a path integral discretization of 160 beads at 0.5 K, while the path integral is discretized using 640 beads for the molecule in conjunction with the PIQTB thermostat. The results reported

here have been obtained by averaging over 20 independent runs propagated using a formal PIMD time step of 0.25 fs for 4×10^5 steps, corresponding to a trajectory length of formally 100 ps for each of the independent runs. Between two PIMD steps, helium was sampled using at least 1×10^5 PIMC moves per helium atom. All interactions involving CH_5^+ and CH_4 are represented using highly accurate neural network potentials (NNPs) trained to essentially converged coupled cluster electronic structure calculations [55,56]. We refer to Appendix A for more information on the methodology of these NNPs as well as for comprehensive benchmarks.

To study the superfluid response of ^4He around the molecule, we compute the superfluid fraction f_s of helium which quantifies the fraction of helium being in the superfluid state. Within the two-fluid model of superfluidity, the total helium density is divided into a superfluid density ρ_s and a normal density ρ_n , and the superfluid fraction is then obtained as the ratio $f_s = \rho_s/\rho_n$. Various estimators have been developed to compute the superfluid fraction in path integral simulations. Here we use the so-called area estimator that has been developed specifically for finite-size clusters [18] and which is based on the vectorial area of the exchange path, see Appendix C 1 for more detailed information. One should note that this estimator is formally valid in the thermodynamic limit and in practice presents some limitations when dealing with very small clusters. In particular, it gives a nonzero superfluid fraction for a single helium atom. This drawback can be corrected using a rescaled estimator, the so-called exchange estimator [29]. We carefully tested the validity of the area estimator in our case, see Appendix C 1 Fig. 18, by comparing to the exchange estimator.

Moreover, to get some local information about the superfluid response of helium, we estimate the local superfluid density $\rho_s(\vec{r})$ in two different ways. The first estimator we use is based on the length of the exchange path. Indeed, it is well-known that superfluidity is related to the presence of long exchange path [57]. It is thus possible to estimate $\rho_s(r)$ by computing the density of long exchange paths [30], $\rho_s(\vec{r}) = \sum_{p>l}^{N_{\text{He}}} \rho_p(\vec{r})$, where the sum runs over exchange paths exceeding a user-defined length of l . In this paper, we chose $l = 6$, i.e., all exchange paths involving more than six atoms are considered to contribute to the superfluid density. We checked that the obtained superfluid densities remain qualitatively similar for different values of the cutoff length, see Appendix C 2, in particular, Fig. 20. The second estimator we use to compute superfluid densities is a generalization of the area estimator of the superfluid fraction, see Appendix C 2 for more details, including the expression and its derivation.

III. STRUCTURAL PROPERTIES

A. Molecular structure

The first question that arises is the impact of the solvent on the molecular properties, in particular, their structure and dynamics. It is usually assumed that the impact of helium is negligible due to the weak nature of its interaction with the molecule, and helium is thus considered one of the best solvents, in particular, for spectroscopic studies [16]. The question of the impact of helium on fluxional molecules, which exhibit fragile large-amplitude motion, has been re-

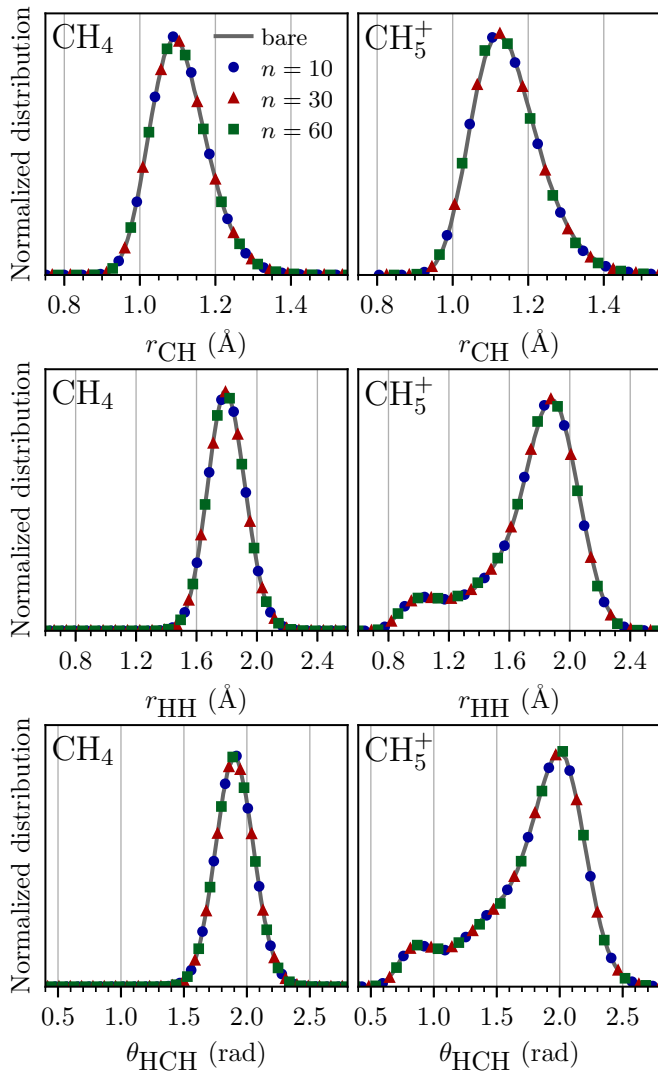


FIG. 1. Molecular structure of CH_4 (left column) and CH_5^+ (right column) solvated by different numbers of helium atoms n (symbols) and compared to the isolated bare $n = 0$ case (gray line) at $T = 0.5$ K. The distributions of CH distances, HH distances, and HCH angles are presented in the top, middle, and bottom panels, respectively.

cently studied for CH_5^+ microsolvated with up to only four ^4He atoms [58]. This study has revealed that the impact of helium on the molecular structure is indeed negligible even for the utmost fluxional CH_5^+ molecule, and that helium does not seem to impact the fluxionality and large-amplitude motion. As clearly seen in the identical distribution functions for the key structural properties of CH_4 and CH_5^+ in Fig. 1, the impact of helium remains negligible, even if the first helium solvation shell is fully closed with 16 helium atoms, probed here with $n = 30$ ^4He . Moreover, no significant change in the molecular structure is observed when increasing the number of helium atoms even up to 60 ^4He around the molecule, in which case the molecule is entirely immersed in helium. Thus, the findings of Ref. [58] are not only valid in the extreme microsolvation limit but extend further to the fully solvated regime.

B. Helium solvation structure

The impact of neutral and charged impurities on the surrounding helium is illustrated by the distributions reported in Fig. 2 for CH_4 versus CH_5^+ solvated by 60 ^4He atoms. The pronounced $\text{CH}_5^+ \cdots ^4\text{He}$ interaction leads to large density modulations around the impurity and almost no interchange of helium atoms between the first and second solvation shells, as seen by the density close to zero in between the two peaks in Fig. 2(d). In contrast, the presence of CH_4 leads to mild modulations even though a weakly defined, faint first shell can be identified followed by a region of significant helium density allowing for easy interchange of ^4He between the first shell and beyond. These are the signatures of the much weaker interaction of ^4He with CH_4 compared to CH_5^+ as a result of CH_5^+ being a charged molecule. This significant impact of CH_5^+ on the solvent structure can also be seen in the $\text{He} \cdots \text{He}$ distributions that indicates a highly structured helium environment only around CH_5^+ whereas not much such structure is seen for CH_4 . This is most pronounced in the first shell, see inset of Fig. 2(e), where the high density of about 0.11 \AA^{-3} , which largely exceeds the freezing density of bulk helium, results in a solidlike order—the ^4He snowball as known from simple monatomic cations. This solidlike structure of the first shell is confirmed by the angular distribution of helium around the carbon atom of CH_5^+ , shown in the inset of Fig. 2(d), that exhibits sharp peaks in the first shell. Finally, the spatial distribution functions (SDFs) depicted in the rightmost column of Fig. 2 clearly summarize what is observed based on these radial and angular distribution functions. The real-space structuring of the probability distribution of ^4He atoms around CH_5^+ versus CH_4 appears clearly: ^4He atoms are significantly more localized around CH_5^+ compared to CH_4 Fig. 2(c), which indicates *pronounced local translational and orientational order of helium close to CH_5^+* . This is what we call solidlike order in such a finite cluster obviously without implying long-range periodicity as in an extended crystal.

Overall, this analysis of the helium structure reveals the presence of a frozen first shell around CH_5^+ . In contrast, this phenomenon is not present for CH_4 , in line with previous work [39], as supported by all data in Figs. 2(a)–2(c). Interestingly, the rovibrational motion of the impurities, even of the strongly interacting CH_5^+ , has a negligible impact on the solvation shell structure for sufficiently large clusters (compare blue to red lines in Fig. 2). This behavior is different in small clusters (see Fig. 14) for which the molecular motion has a significant impact on the helium solvation structure. A pictorial summary of the structural differences is provided by the different SDFs in Fig. 2: While the 3D distribution of ^4He around CH_4 in Fig. 2(c) is broad and smeared out (liquidlike), ^4He atoms are localized at a well-defined position (solidlike) around CH_5^+ in Fig. 2(f).

IV. SUPERFLUID PROPERTIES

How are these structural differences linked to the superfluid response of ^4He , f_s , as a function of the number n of ^4He atoms? Within the two-fluid model of superfluidity, the superfluid fraction f_s is defined as the ratio between the superfluid density ρ_s and the total density ρ . It can be obtained

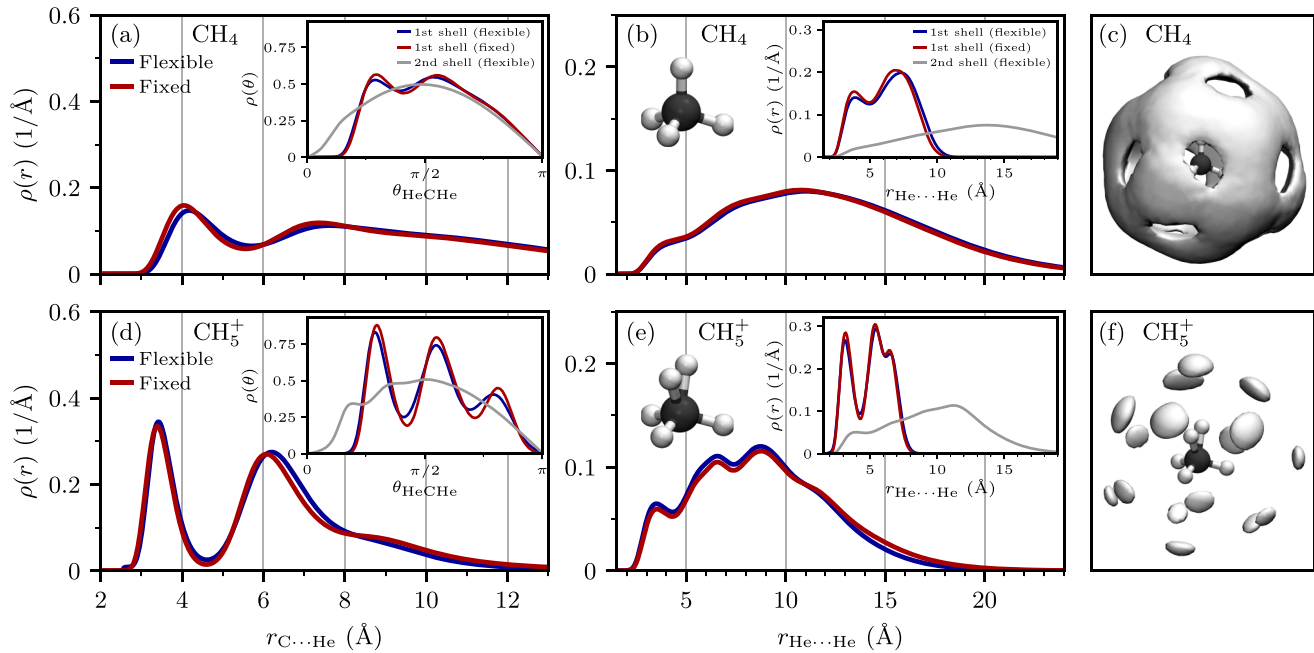


FIG. 2. Distance distribution functions of $C \cdots He$ [(a), (d)] and $He \cdots He$ [(b), (e)] distances as well as spatial distribution functions (SDFs) of 4He around the impurities [(c), (f)] for $CH_4 \cdot {}^4He_{60}$ (top row) and $CH_5^+ \cdot {}^4He_{60}$ (bottom row); data for the fully flexible and completely fixed impurities [with all constituting nuclei frozen as point particles at their equilibrium structures as depicted in the insets of (b) and (e)] are shown in blue and red, respectively. The insets of (a) and (d) depict the angular distribution functions of 4He with respect to the carbon atom in the first and second (gray) shells, whereas the insets of (b) and (e) show the $He \cdots He$ distance distributions split into first and second (gray) shells. The SDFs have been computed with respect to fixed impurities using isovalues corresponding to a third of the respective maximum value which highlights the first 4He shell.

directly from our quantum simulations and, in addition, spatially decomposed in terms of local shell contributions based on the radial superfluid density $\rho_s(r)$, see the Appendix C for methods. Figure 3 shows the global superfluid fraction of the helium around CH_4 and CH_5^+ as a function of the number of helium atoms. For CH_4 , f_s increases with n before reaching a maximum at $n = 9$ which corresponds to the maximum size for which all helium atoms mostly belong to the first shell, as shown in Fig. 16. After that, f_s drops initially due to the low density of additional helium atoms outside the first shell which hinders bosonic exchange. Upon filling the second shell, f_s increases again, reaching about 0.78 for the largest cluster. As for the helium densities, the rovibrational motion of CH_4 has a negligible impact on f_s around this quasirigid and weakly interacting molecule as fixing its nuclei (red diamonds compared to blue squares) does not change f_s . We note that we obtain very similar values of f_s at $T = 0.3$ K (flexible: 0.91, fixed: 0.88) as reported for 12 helium atoms around CH_4 in Ref. [39].

The superfluid response around CH_5^+ is distinctly different. Despite the strongly localized helium in the first shell, recall Fig. 2(f) versus Fig. 2(c), a large superfluid fraction, exceeding even the largest value obtained for the weakly interacting CH_4 , is found around the CH_5^+ impurity. Moreover, neglecting the rovibrational motion by fixing CH_5^+ now greatly suppresses f_s , indicating almost no superfluid response for clusters of size lower than around 30 4He atoms (red triangles compared to blue circles) as expected from the tra-

ditional snowball picture. In the limit of large clusters, the *global* superfluid fraction tends to unity, which is expected regardless of the impurity since 4He is indeed superfluid at this temperature and we thus retrieve the bulk limit. In other words, for CH_4 , the superfluid fraction does not change whether we fix the molecule in its equilibrium structure or not. This indicates that there is no impact of the rovibrational motion of CH_4 on the superfluid response of the surrounding helium. In stark contrast, in the case of CH_5^+ , the superfluid fraction values obtained when fixing the molecule in space are extremely small compared to the large values found when allowing for full flexibility of the molecule. This shows that, in the case of protonated methane, the rovibrational motion of the molecule plays a crucial role and actually considerably enhances the superfluid response of the surrounding helium—despite the pronounced *local translational and orientational order of helium observed in the first shell around CH_5^+* .

A deeper understanding can be obtained by studying the bosonic exchange path statistics for flexible versus fixed molecular impurities, see Fig. 3. The rovibrational motion of the fluxional CH_5^+ significantly enhances bosonic exchange and facilitates long exchange cycles that are known to be related to superfluidity [30,57]. No such impact on bosonic exchange is observed for the neutral CH_4 .

Studying the evolution of the superfluid fraction with cluster size $n \geq 6$ in Fig. 3, one can see that in the case of flexible CH_5^+ , $f_s \approx 1$ for $n = 6$ to 16 which corresponds to the first shell being completely filled (except for a drop at

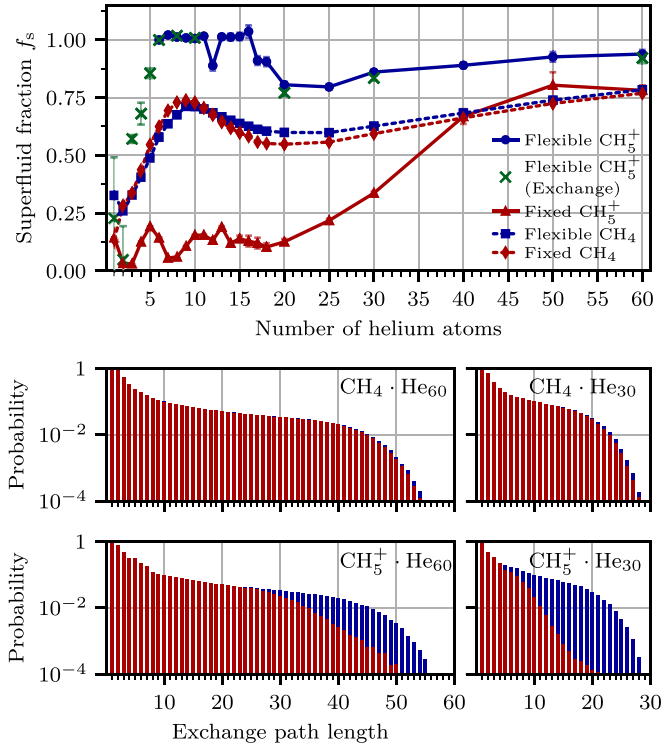


FIG. 3. Top: Superfluid fraction f_s for $\text{CH}_4 \cdots {}^4\text{He}_n$ (dashed lines) and $\text{CH}_5^+ \cdot \text{He}_n$ (solid lines) as a function of n ; the exchange estimator has been used to compute the green crosses whereas all other data have been obtained from the area estimator as explained in Appendix C 1 and validated in Fig. 18. Bottom: Probability of finding at least one exchange path of specific length for $n = 60$ (left) and $n = 30$ (right) ${}^4\text{He}$ atoms. Data for flexible and fixed impurities (see caption of Fig. 2) are shown in blue and red, respectively; note that blue is superimposed by red where not visible.

$n = 12$, which is due to a known topological phenomenon as explained in Appendix C based on Fig. 19). After that, the value of f_s is slightly reduced due to the buildup of a second shell with a locally reduced ${}^4\text{He}$ density that disfavors bosonic exchange. Upon increasing n , the second shell gets filled and f_s increases accordingly, reaching $f_s \approx 0.9$ for $n = 60$, see Fig. 16 for shell-filling analysis. Our analyses indicate that the first solvation shell of ${}^4\text{He}$ around flexible CH_5^+ features maximum superfluidity as quantified by $f_s \approx 1$. Such a pronounced superfluid response is found despite the first shell being solidlike.

Spatially resolved insights into the superfluid response of helium can be obtained by defining a local superfluid density $\rho_s(r)$ as presented in Fig. 4 for two different local estimators; see SM Sec. III B [59] for an extended discussion and validation. Similarly to what was observed for the superfluid fraction, the rovibrational motion of CH_4 has a negligible impact on the superfluid density from the first shell up to the largest $\text{C} \cdots \text{He}$ distances. For CH_5^+ , a very different scenario is found: Essentially zero superfluid density is present in the first ${}^4\text{He}$ shell around the fixed CH_5^+ molecule compared to a significant superfluid response in the second shell as clearly seen in the shell-resolved integrated superfluid densities in Table I. This is a direct consequence of the solidlike or-

der of the helium in the first shell—induced by the strong interactions of this cationic impurity with helium—that suppresses the long exchange cycles and thus the superfluid response. When accounting for the rovibrational motion of this molecule, however, the superfluid response of the first shell considerably increases. These findings are consistent between the two different local estimators of superfluidity as presented in the top and bottom panels of Fig. 4 as well as Table I. The main difference between the two estimators is the extent of superfluidity, where the exchange path estimator yields overall lower estimates throughout compared to the area estimator. By construction, the exchange path length estimator will always tend to underestimate the superfluid response while the area estimator is expected to overestimate it, so ultimately the “real” superfluid density lies somewhere in between. For further details and an in-depth discussion, we refer to Appendix C 2.

Importantly, this enhancement of the superfluid response of the first shell is not due to a decrease of the local solidlike order in the first shell as one could imagine, since the solvation structure is unaffected by the rovibrational molecular motion of CH_5^+ as shown in Fig. 2. In a nutshell, in view of the strong localization of helium in the first shell around CH_5^+ , one would expect almost no superfluid response as obtained around other strongly interacting impurities that lead to snowballs, and that is what is found when fixing that molecule in its equilibrium structure. However, including the full flexibility of CH_5^+ , high superfluid fractions are found, in particular, in the first shell, thus showing that the superfluid response of helium is induced by the rovibrational motion of this flexible molecule despite the pronounced localization of ${}^4\text{He}$ close to this impurity.

We therefore conclude that helium in the first solvation shell around CH_5^+ features *manifestations of supersolid behavior* (in the spirit of *manifestations of superfluid behavior* predicted long ago for *pure* ${}^4\text{He}$ clusters [18]) as indicated by pronounced bosonic exchange in combination with strong localization and spatial order of ${}^4\text{He}$. Evidently, the phenomenon uncovered here can only appear for clusters that are large enough to fully solvate the impurity and is thus absent in the microsolvation limit.

Are there any prospects to experimentally probe our prediction? Manifestations of superfluid behavior in finite ${}^4\text{He}$ clusters were initially predicted based on seminal path integral simulations [18] and experimentally confirmed a decade later. This experimental confirmation of *microscopic manifestation of superfluidity* was made possible thanks to experimental ideas based on the IR spectra of a well-chosen molecular impurity used as probe of the local superfluidity in ${}^4\text{He}$ clusters [15]. Concerning now manifestations of local supersolidity in $\text{CH}_5^+ \cdot \text{He}_n$ clusters, we refer to recent progress in measuring IR spectra of various charged molecules in helium clusters and nanodroplets [46,60–62], notably also including CH_5^+ . Similar to the original ideas behind what has been called the microscopic Andronikashvili experiment [15], IR spectra of CH_5^+ in ${}^3\text{He}$ versus ${}^4\text{He}$ nanodroplets as well as addition of a few ${}^4\text{He}$ atoms to CH_5^+ in ${}^3\text{He}$ could reveal insightful differences. Challenges certainly arise regarding IR spectroscopy of CH_5^+ since the molecule is known to stay fluxional in helium [46,47,58] thus retaining its notorious spectroscopic complexity [63]. Exploring alternative observables different from IR

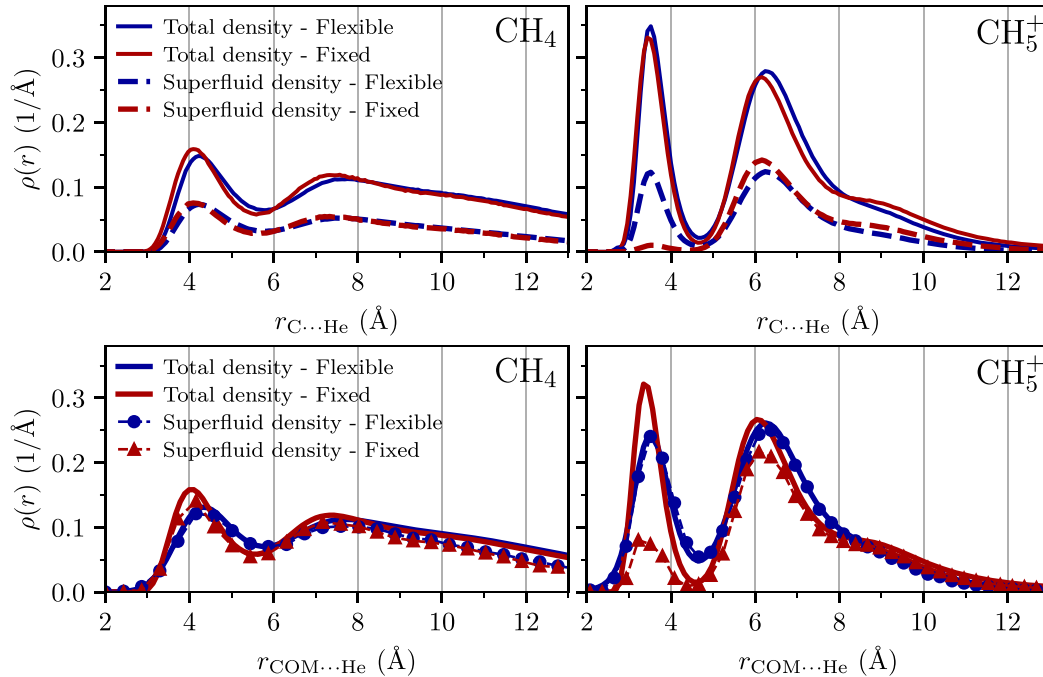


FIG. 4. Local superfluid density $\rho_s(r)$ computed using the local exchange path estimator (top row: dashed line) considering seven or more ${}^4\text{He}$ atoms ($l = 6$), and using the local area path estimator (bottom row: dashed line with symbols), together with the radial total density $\rho(r)$ (full line). Data for the flexible and fixed impurities (see caption of Fig. 2) are shown in blue and red, respectively. Note that the definition of the radial density in the top and bottom panels is slightly different: In the top panels, the distance r is defined with respect to the central carbon atom of the molecule, while in the bottom panel it is with respect to the center of mass of the molecule as indicated in the axis labels.

TABLE I. Global superfluid fraction f_s and local superfluid fractions associated with the first and second solvation shells of $\text{CH}_4 \cdot \text{He}_{60}$ and $\text{CH}_5^+ \cdot \text{He}_{60}$ obtained by integrating the superfluid density computed using either the local area estimator or the local exchange path estimator with a cutoff length of $l = 6$, see Appendix C 1 for details.

$\text{CH}_4 \cdot \text{He}_{60}$: Flexible molecule			
	First shell	Second shell	Global
Exchange path	0.74	0.59	0.63
Area	0.96	0.83	0.86
$\text{CH}_4 \cdot \text{He}_{60}$: Fixed molecule			
	First shell	Second shell	Global
Exchange path	0.72	0.59	0.63
Area	0.90	0.82	0.84
$\text{CH}_5^+ \cdot \text{He}_{60}$: Flexible molecule			
	First shell	Second shell	Global
Exchange path	0.54	0.63	0.61
Area	0.99	0.95	0.96
$\text{CH}_5^+ \cdot \text{He}_{60}$: Fixed molecule			
	First shell	Second shell	Global
Exchange path	0.04	0.55	0.42
Area	0.28	0.83	0.68

spectra might therefore provide complementary avenues for future experimental searches for this local supersolidity in doped He^4 clusters potentially based on experimental ideas that are yet to be developed.

V. CONCLUSIONS AND OUTLOOK

This paper provides strong evidence for manifestations of local supersolid behavior of ${}^4\text{He}$ around a charged molecular impurity, namely, CH_5^+ . On the one hand, the strong interactions between this molecular cation and helium lead to the long-known snowball effect, meaning a solidlike arrangement of helium in the first shell with well-localized ${}^4\text{He}$ density. On the other hand, the strongly localized atoms in this shell are involved in vivid bosonic exchange, induced by the rovibrational motion of this fluxional molecular impurity, in particular, the fast and complex rotational motion emerging from the intimate coupling of overall rotations and intramolecular pseudo-rotations. The combination of strong ${}^4\text{He}$ localization in the first shell with pronounced bosonic exchange therein, leading to an intense superfluid response, thus clearly indicates manifestations of local supersolid behavior of ${}^4\text{He}$ close to suitable molecular impurities—akin to the long-known manifestations of microscopic superfluidity in doped helium nanodroplets.

We expect this impurity-induced local supersolid response to appear in bosonic clusters doped with other impurities

featuring a strong interaction with the solvent combined with fast rotations, resulting in a significant coupling between the impurity and the solvent. In particular, due to the stronger interactions of most impurities with para-H₂, we believe that the effect uncovered here could appear as well in finite para-H₂ clusters doped with molecular impurities. The phenomenon is, however, markedly different from the supersolidity that has long been predicted in pure para-H₂ clusters of specific sizes, since the local supersolid behavior is induced here by the molecular impurity and is also not limited to magic numbers. Moreover, since the effect uncovered here can be expected to appear with various molecular ions in helium or other bosonic quantum fluids, it would be highly interesting to explore, in particular, whether doping with an assembly of molecular ions serving as seeds could lead to unique supersolid phases, especially in bulk helium or parahydrogen.

ACKNOWLEDGMENTS

We are thankful to H. Forbert and F. Uhl for many insightful discussions. This work was partially supported by DFG via MA No. 1547/19 and also funded by the Deutsche Forschungsgemeinschaft (DFG, German Research Foundation) under Germany's Excellence Strategy—EXC 2033—No. 390677874. C.S. acknowledges partial financial support from the Alexander von Humboldt-Stiftung and DFG Project No. 500244608. The computational resources were provided by HPC@ZEMOS, HPC-RESOLV, and BoVi-Lab@RUB. We acknowledge support by the Open Access Publication Funds of the Ruhr-Universität Bochum.

APPENDIX A: NEURAL NETWORK POTENTIALS

1. Methodology

High-dimensional NNPs [64,65] have been fitted against coupled cluster reference calculations including singles, doubles, and perturbative triple excitations, CCSD(T). The augmented correlation-consistent basis set up to triple zeta functions [66,67] (aug-cc-pVTZ or AVTZ) has been used in combination with the explicitly correlated F12a method [68,69] using an adequate scaling of the triples [69] [providing CCSD(T*)-F12a/AVTZ, which is referred to simply as CC in the following], leading to a description of the electronic structure that is essentially converged to the complete basis set limit. All reference calculations have been performed with the MOLPRO software package version 2012.1 [70]. The iterative procedure described in Refs. [55,56] was used to optimally build the training sets of the models, while ensuring that only a minimum number of reference calculations were performed. All atomic neural networks have a fully connected feed-forward architecture composed of two hidden layers of 25 nodes each using a hyperbolic tangent as the activation function. The output layer contains only one neuron activated by a linear function as usual for regression. Training of the models was performed with the RUNNER program [71] using the element-decoupled Kalman filter optimizer [72]. The local atomic environments used as inputs of the models are described by atom-centered symmetry functions [73]. We refer to the supporting file `nnp-parameters.pdf`, where all parameters of all NNPs as used in this paper are provided.

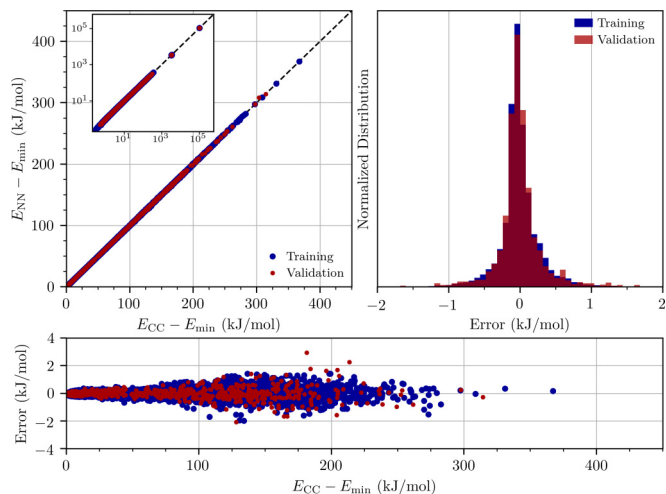


FIG. 5. Analysis of the training of the CH₅⁺ NN-PES. Correlations of the energies obtained by the NN-PES (NN) and the reference coupled cluster (CC) method (top left). Histogram (top right) and values (bottom) of the associated errors. The energies are reported relative to the energy of the global minimum E_{\min} .

The interactions between the molecules and helium are described by separate NNPs that were fitted to reproduce the impurity...He interaction in a pairwise manner [55]. The reference interaction energies have been computed at the same level of theory as for the potential energy surfaces (PES) of the molecules, but using the supermolecule approach and a counterpoise correction (cp) to correct for the basis set superposition error [74] [thus providing the CCSD(T*)-F12a-AVTZcp method, which we also refer to as CC for simplicity in what follows]. The scaling correction of the triple excitations has been applied in a system-size-consistent manner [75] by determining the correction only from the supermolecular cluster.

2. Potential energy surface of CH₅⁺

The training of the NNP to describe the PES of CH₅⁺, thus providing what we call the NN-PES (NN-PES-CH5P-2022-V0), was performed on a training set composed of 18 266 configurations as sampled by our automated fitting procedure from MD with classical nuclei and PIMD simulations considering nuclear quantum effects at various temperatures ranging from 1 up to 1500 K. A limited amount of CH₃⁺ and H₂ configurations were added to correctly describe configurations that are close to the dissociation channel (adding up to 800 CH₃⁺ and 32 H₂ representative structures). Ten percent of the data set is used as a validation set to assess the quality of the fit and to detect overfitting. The root mean square error (RMSE) obtained for the training and validation set is 0.3 and 0.4 kJ/mol, respectively, and the overall high quality of the training is illustrated in Fig. 5. The final NN-PES has been validated by investigating important stationary-point structures of protonated methane represented by the minimum energy structure and the lowest two saddle points depicted in Fig. 6. The global minimum energy structure of CH₅⁺ has an eclipsed C_s (e - C_s) point symmetry and is composed of a CH₃ tripod and a H₂ moiety connected through a three-center

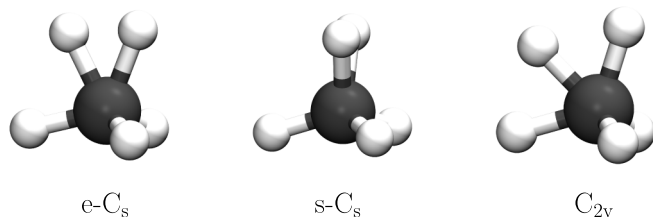


FIG. 6. Important structures of CH_5^+ : Minimum energy (left), first stationary point (center), and second stationary point (right).

two-electron bond [44]. This H_2 moiety can rotate around the C_3 axis of the tripod, a motion associated to a stationary point with staggered C_s ($s - C_s$) symmetry and a small energy barrier that makes this pseudorotation essentially barrier-free. The second low-lying stationary point has C_{2v} symmetry and is associated with another pseudorotation that connects two degenerate $e - C_s$ structures involving different atoms in the moiety. The combination of these two pseudorotations leads to a large-amplitude motion, sometimes called scrambling motion, that makes all the hydrogen atoms dynamically equivalent. Since this scrambling motion is associated with tiny energy barriers that are overcome by zero-point energy, CH_5^+ exhibits large-amplitude motion even in the $T \rightarrow 0$ limit: Protonated methane is the typical example of a quantum fluxional molecule.

Geometry optimizations of these different structures of CH_5^+ have been performed using both the NN-PES and explicit CC reference calculations. Their relative energies are compared in Table II to confirm that the energy barriers associated with the large amplitude motion of protonated methane are correctly reproduced by the NN-PES. In particular, these tests show that the NN-PES represents the stationary points of CH_5^+ on its complex PES to very high precision, which greatly exceeds chemical accuracy. Moreover, the normal mode frequencies of CH_5^+ in the minimum energy structure have been computed with the NN-PES and are compared in Table III to the values obtained with the CC reference method. Also here, the NN-PES is able to reproduce the CC reference within a few cm^{-1} , highlighting the quality of this approach.

Finally, to further test the NN-PES on structures actually sampled in realistic simulations, we randomly extracted short pieces of MD and PIMD trajectories of a single CH_5^+ in the gas phase in which the potential energy was evaluated using both the NN-PES and the CC reference method as depicted in Fig. 7. Independent of whether the nuclei are described as classical point particles or including nuclear quantum effects, the NN-PES provides perfect agreement with the CC reference energies covering very different temperature regimes.

TABLE II. Energy difference $\Delta E(X) = E(X) - E(e - C_s)$ in kJ/mol as obtained using the NN-PES and the reference CC method with associated errors.

X	NN	CC	Error
$s - C_s$	0.3855	0.4296	0.0441
C_{2v}	3.817	3.6559	-0.1611

TABLE III. Normal mode frequencies in cm^{-1} in the minimum energy $e - C_s$ structure of CH_5^+ as obtained using the NN-PES and the reference CC method with associated errors. The mean absolute deviation (MAD) is also reported on the last line.

NN	226.48	831.19	1284.52	1301.37	1460.18	1482.71
CC	211.92	828.23	1282.81	1289.30	1461.79	1490.27
Error	-14.56	-2.96	-1.71	-12.1	1.61	7.56
NN	1590.29	2436.55	2720.25	3004.74	3135.13	3238.15
CC	1595.63	2449.88	2713.51	3014.75	3133.99	3228.55
Error	5.34	13.3	-6.74	10.0	-1.14	-9.60
MAD	7.2					

These various tests clearly highlight the outstanding quality of this NN-PES of CH_5^+ that essentially allows for a description of the molecule at converged coupled cluster accuracy.

3. Potential energy surface of CH_4

The NN-PES of CH_4 (NN-PES-CH4-2022-V0) has been developed following the same automated fitting procedure as used for CH_5^+ . The data set generated here is composed of 9245 configurations which have been selected from both PIMD and MD trajectories of isolated CH_4 at temperatures ranging from 1.67 up to 1000 K. The RMSE associated with the training of the NN-PES are 0.02 kJ/mol for the training set and 0.03 kJ/mol for the validation set. The quality of the fit is further illustrated in Fig. 8 at the level of errors, which clearly highlights that fitting the NN-PES of such a quasi-rigid and symmetric molecule as CH_4 is a much easier task than fitting the complex PES of highly fluxional molecules such as CH_5^+ . The minimum energy structure is very well reproduced with an error on the energy that is lower than 0.05 kJ/mol and errors on the associated normal modes of

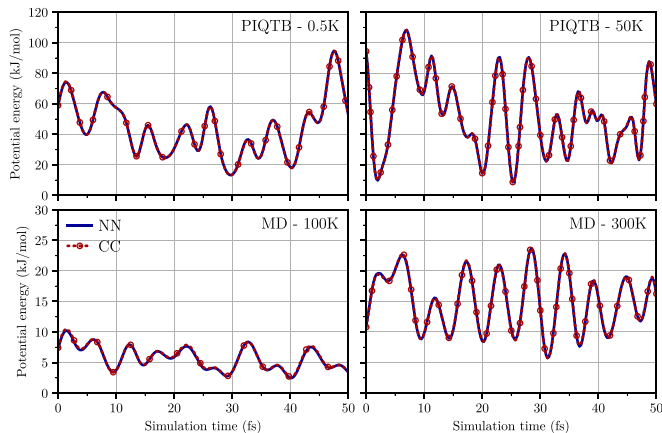


FIG. 7. Potential energy of an isolated CH_5^+ molecule along one replica of PIQTB trajectories (first row) at $T = 0.5$ K (left) and 50 K (right) and along a standard MD trajectory (second row) at $T = 100$ K (left) and 300 K (right). The coupled cluster reference data (CC) were obtained by recomputing the energies at each step of the NN-PES trajectories and are shown as red dashed lines (with only a few circles added since the CC energies practically superimpose the NN-PES data). All energies are reported relative to the energy of the global minimum ($e - C_s$).

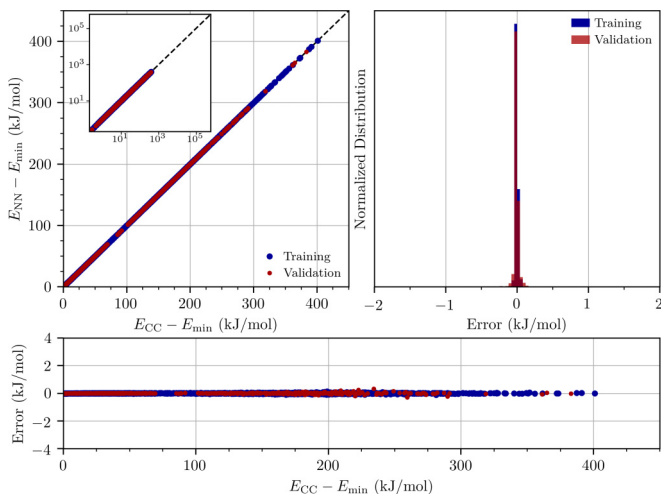


FIG. 8. Analysis of the training of the CH_4 NN-PES. Correlations of the energies obtained by the NN-PES (NN) and the reference coupled cluster (CC) method (top left). Histogram (top right) and values (bottom) of the associated errors. The energies are reported relative to the energy of the global minimum E_{\min} . We employ here, on purpose, the same scale as used for the validation of the CH_5^+ NN-PES analyzed in Fig. 5 to allow for one-to-one comparison of these two cases which represent quasirigid (CH_4) and highly fluxional (CH_5^+) molecules of very similar kind and size.

around 1 cm^{-1} only, as compiled in Table IV. As for CH_5^+ , the quality of the NN-PES is further tested on short parts of representative MD and PIMD trajectories obtained using the NN-PES for which the potential energy gets reevaluated using the reference CC method, see Fig. 9. For all these validation simulations—including various temperatures and both classical and quantum nuclei—essentially perfect agreement between the NN-PES and the CC reference is observed.

4. $\text{CH}_5^+ \cdots \text{He}$ interaction

The $\text{CH}_5^+ \cdots \text{He}$ interaction has been parameterized in terms of a NN-PES (NN-IP-CH5P-HE-2022-V0) using another automated procedure as described in Ref. [55], which is similar to the one used for fitting the molecular PES but deviating in crucial aspects as explained previously. The data set used for this purpose is composed of 48000 $\text{CH}_5^+ \cdots \text{He}$ configurations. The RMSE associated with the training and validation set is 0.03 and 0.05 kJ/mol, respectively, and the

TABLE IV. Normal mode frequencies in cm^{-1} in the minimum energy structure of CH_4 as obtained using the NN-PES and the reference CC method with associated errors. The mean absolute deviation (MAD) is also reported on the last line.

NN	1344.04	1344.04	1344.04	1568.65	1568.65
CC	1343.20	1343.32	1343.37	1568.09	1568.20
Error	-0.84	-0.72	-0.67	-0.56	-0.45
NN	3036.86	3156.00	3156.00	3156.00	3156.00
CC	3032.68	3155.17	3155.26	3155.36	3155.36
Error	-4.18	-0.83	-0.78	-0.64	
MAD	1.1				

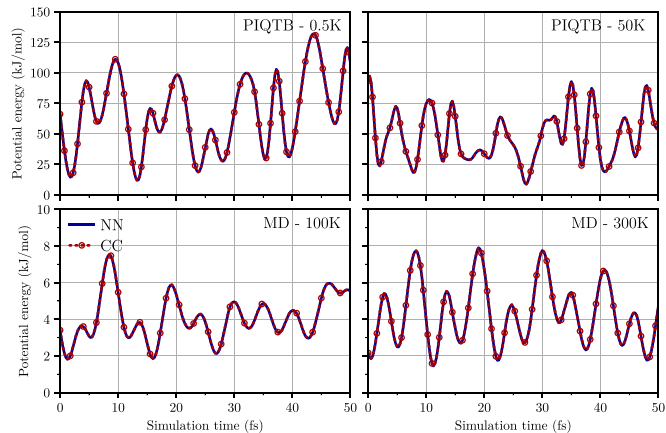


FIG. 9. Potential energy of an isolated CH_4 molecule along one replica of PIQTB trajectories (first row) at $T = 0.5 \text{ K}$ (left) and 50 K (right) and along a standard MD trajectory (second row) at $T = 100 \text{ K}$ (left) and 300 K . The coupled cluster reference data (CC) were obtained by recomputing the energies at each step of the NN-PES trajectories and are shown as red dashed lines (with only a few circles added since the CC energies practically superimpose the NN-PES data). All energies are reported relative to the energy of the global minimum.

quality of the fit is illustrated in Fig. 10. To further test this neural network description of the $\text{CH}_5^+ \cdots \text{He}$ interactions, we put it to a most stringent test by directly comparing the helium density (in terms of its SDF) obtained using the NN-PES and the CC reference method around a space-fixed molecular impurity. In practice, the interaction potential is first tabulated on a fine grid around the fixed molecule: For each point, the interaction energy is computed using both the NN-PES and the CC method. PIMC simulations of helium around the molecule are then performed using the precomputed energy value on the closest grid point. This allows us to compute approximate helium densities in Cartesian space around a fixed molecular impurity—even with the computa-

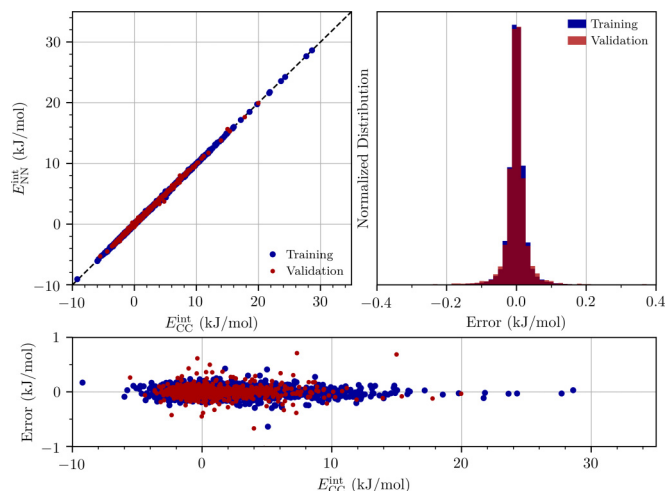


FIG. 10. Analysis of the training of the $\text{CH}_5^+ \cdots \text{He}$ NN-PES. Correlations of the interaction energies obtained by the NN-PES (NN) and the reference coupled cluster (CC) method (top left). Histogram (top right) and values (bottom) of the associated errors.

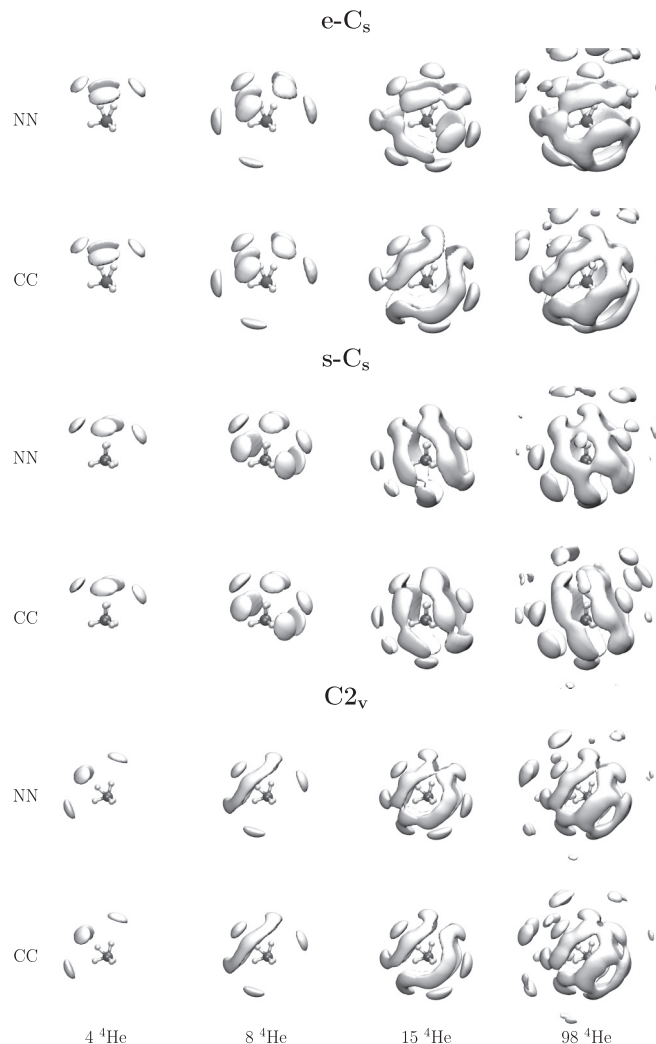


FIG. 11. Helium densities (spatial distribution functions) around CH_5^+ completely fixed in space in various representative configurations, $e-C_s$ (first two rows), $s-C_s$ (third and fourth rows), and C_{2v} (last two rows). The densities are computed by PIMC at $T = 1.67$ K without bosonic exchange and using potential energy values that have been precomputed with the NN-PES (NN) and the reference coupled cluster method (CC) on a fine grid around the fixed molecule. Isosurface values: $0.035 N_{\text{He}}/\text{\AA}^3$ for 4 He, $0.025 N_{\text{He}}/\text{\AA}^3$ for 8 He, $0.020 N_{\text{He}}/\text{\AA}^3$ for 15 He, and $0.015 N_{\text{He}}/\text{\AA}^3$ for 98 He.

tionally expensive CC method. The results of this comparison are presented in Fig. 11 and clearly show that the NN-PES correctly reproduces the helium densities around CH_5^+ in all important configurations, namely, $e-C_s$, $s-C_s$, and C_{2v} , even for a large number of helium atoms (98 atoms here). Upon closer inspection, one can detect some small remaining differences for large numbers of ^4He atoms (where smaller isovalues are required to visualize the larger clusters) around CH_5^+ in the $e-C_s$ configuration; a similar observation has been made and analyzed earlier [55] in Figs. 3 and 4 therein. Nevertheless, the most prominent features of the density remain correctly described even for 98 helium atoms and the NN-PES, and thus, still provide an accurate description of the helium density in these cases.

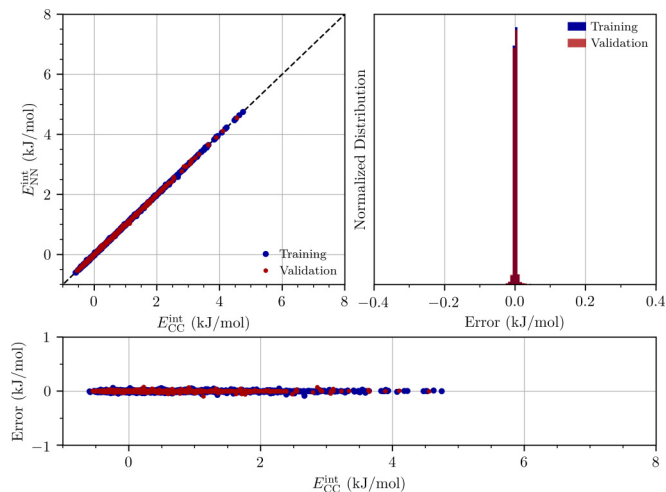


FIG. 12. Analysis of the training of the $\text{CH}_4 \cdots ^4\text{He}$ NN-PES. Correlations of the interaction energies obtained by the NN-PES (NN) and the reference coupled cluster (CC) method (top left). Histogram (top right) and values (bottom) of the associated errors.

5. $\text{CH}_4 \cdots$ helium interaction

As for $\text{CH}_5^+ \cdots ^4\text{He}$, we use a dedicated high-dimensional NNP to describe the $\text{CH}_4 \cdots ^4\text{He}$ interaction potential (NN-IP-CH4-HE-2022-V0). The generation of the data set as well as the training of the interaction potential are performed using the same automated approach as before. The data set is composed of 47 833 $\text{CH}_4 \cdots ^4\text{He}$ configurations and the RMSE associated with the training and validation set is 0.004 and 0.005 kJ/mol, respectively. The quality of the fit is illustrated in Fig. 12, which clearly shows that the NN-PES is able to reproduce the CC reference to very high precision. To further test this description of the $\text{CH}_4 \cdots ^4\text{He}$ interaction, we put it to the same test as before and directly compare the helium densities obtained using the NN-PES and the CC reference method around a fixed molecular impurity in the minimum energy configuration. The results presented in Fig. 13 clearly show that this approach is again able to describe the helium solvation of the molecule with great accuracy since essentially no difference between the densities can be observed.

APPENDIX B: SOLVATION SHELL STRUCTURE

In addition to the structural properties presented in the main text, here we present further details of the structure of the helium solvation shell. Various distributions are presented in Fig. 14, which show that helium around CH_5^+ is much more structured than around CH_4 , an effect that is the direct result of the much stronger interaction between helium and protonated methane as quantified in Fig. 15. One can also see from the distributions in Fig. 14 that completely neglecting the molecular degrees of freedom by fixing the two molecules at their minimum energy configurations does not qualitatively change the helium solvation shell structure for large clusters. In particular, in the large cluster limit, $n = 60$, the impact of molecular motion on the overall structure of the solvation shell is essentially negligible. Focusing more closely on the

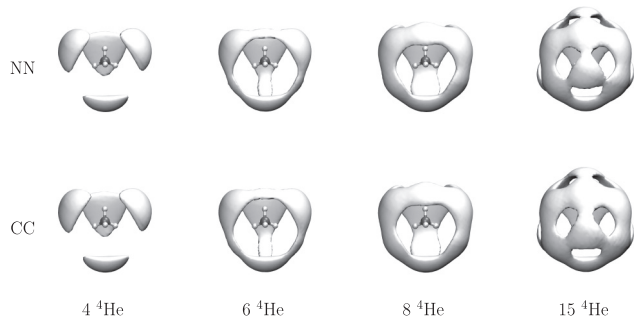


FIG. 13. Helium densities (spatial distribution functions) around CH_4 completely fixed in space in its minimum energy configuration. The densities are computed by PIMC at $T = 1.67$ K without bosonic exchange and using potential energy values that have been precomputed with the NN-PES (NN) and the reference coupled cluster method (CC) on a fine grid around the fixed molecule. Isosurface values: $0.0040 N_{\text{He}}/\text{\AA}^3$ for 4 and 6 He, $0.0050 N_{\text{He}}/\text{\AA}^3$ for 8 He, and $0.0055 N_{\text{He}}/\text{\AA}^3$ for 15 He.

$\text{C} \cdots \text{He}$ distance distributions, a clear shell structure appears around CH_5^+ featuring a sharp first solvation shell localized between 2.5 and 4.8 \AA , which is filled with 16 ^4He atoms as analyzed in detail in Fig. 16. In the case of CH_4 , however,

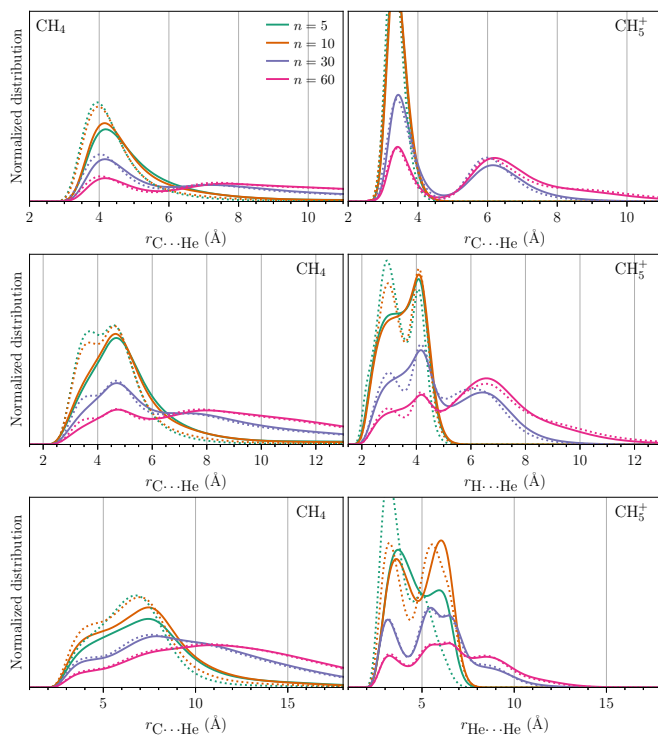


FIG. 14. Structure of the helium solvation shell around CH_4 (left column) and CH_5^+ (right column) for different numbers n of ^4He atoms at $T = 0.5$ K. The dotted lines correspond to molecules completely fixed in space in their minimum energy structures. The first column presents distributions of $\text{C} \cdots \text{He}$ distances, the second column presents distributions of $\text{H} \cdots \text{He}$ distances, and the last column presents distributions of $\text{He} \cdots \text{He}$ distances. All the distributions are normalized to unity.

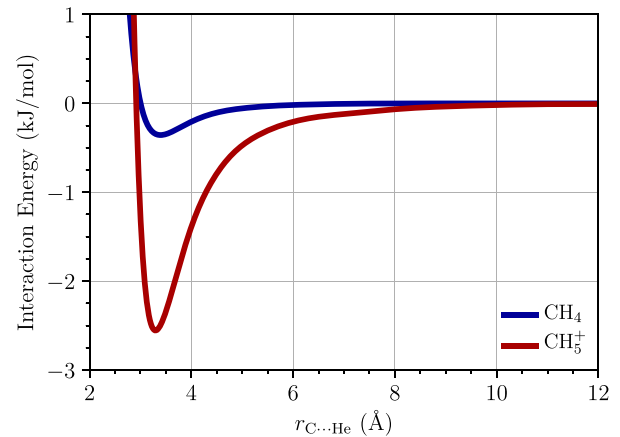


FIG. 15. Interaction energy as a function of the $\text{C} \cdots \text{He}$ distance along the direction of maximum interaction for both CH_4 and CH_5^+ fixed in their minimum energy structure.

only a faint shell structure is observed with a first shell that is much less clearly defined and located between around 2.75 and 5.9 \AA . Studying the evolution of the $\text{C} \cdots \text{He}$ distance as a function of the number of helium atoms n in Fig. 16

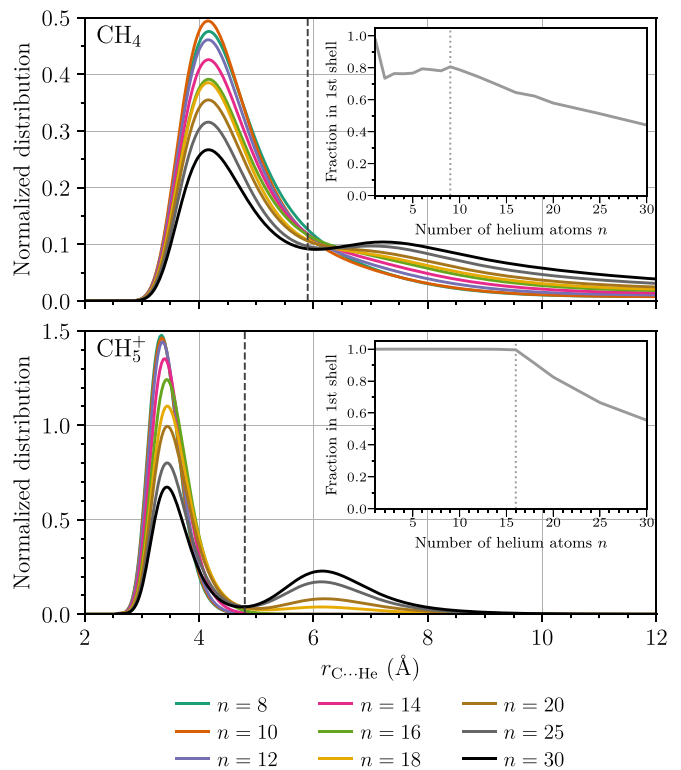


FIG. 16. Distribution of $\text{C} \cdots \text{He}$ distances around CH_4 (top) and CH_5^+ (bottom) at $T = 0.5$ K for different numbers of helium atoms n as provided below the plots. The insets show the fraction of helium atoms that are in the first shell as a function of the number of ^4He atoms n computed by integrating the density in the first shell; the vertical dotted lines indicate the n values when the second shell starts to be gradually filled. The distance used to separate between first and second shell is 5.9 \AA for CH_4 and 4.8 \AA for CH_5^+ as marked by the dashed vertical lines in the main plots.

shows that a second shell is formed around CH_5^+ for $n > 16$ ^4He atoms; see, in particular, the corresponding inset. The situation is, however, less clear around CH_4 where a second shell can only be hinted for $n > 20$ ^4He atoms. When looking at the fraction of atoms that form the first shell it is evident that the second shell already starts to be gradually filled for $n > 9$ ^4He atoms around CH_4 , as seen in the inset of Fig. 16, whereas shell filling is sharp in the case of the strongly interacting CH_5^+ molecule.

APPENDIX C: SUPERFLUID ESTIMATORS

1. Superfluid fraction

Within the two fluid model of superfluidity, the density of helium ρ is divided into a superfluid component ρ_s and a normal component ρ_n with

$$\rho = \rho_n + \rho_s. \quad (\text{C1})$$

The superfluid fraction can then be defined as the fraction of helium in the superfluid state $f_s = \rho_s/\rho$ and is connected to the decrease of the effective moment of inertia I^{eff} that appears at temperatures lower than the critical temperature T_c of the superfluid transition,

$$f_s = 1 - f_n = 1 - \frac{I^{\text{eff}}(T < T_c)}{I^{\text{eff}}(T = T_c)}, \quad (\text{C2})$$

with $f_n = \rho_n/\rho$ being the normal fraction. This formula can, of course, only be used in cases where a proper superfluid phase transition appears for which a critical temperature can unambiguously be defined, as done experimentally for bulk ^4He at ambient pressure (while assuming that the total density does not change as a function of temperature in that range). In this case, $T_c = 2.17$ K is the standard critical temperature of the lambda transition.

In the famous Andronikashvili experiment [76], the effective moment of inertia is measured through the angular frequency of a torsional oscillator immersed in liquid helium. Upon decreasing temperature, the contribution of the helium to the total moment of inertia, i.e., the effective moment of inertia, decreases and reaches zero when the helium is entirely superfluid ($f_s = 1$). In simulations, the effective moment of inertia can be obtained using the following relation from linear response theory:

$$I_\alpha^{\text{eff}} = \left. \frac{\partial \langle \hat{L}_\alpha \rangle}{\partial \omega} \right|_{\omega=0}, \quad (\text{C3})$$

that connects the α principal component of the effective moment of inertia to the response of helium to an infinitesimally slow rotation around the principal \vec{e}_α axis; note that any axis can be taken in the homogeneous isotropic bulk limit. Within the path integral framework, Eq. (C3) can be used to obtain the following expression for the effective moment of inertia:

$$I_\alpha^{\text{eff}} = I_\alpha^{\text{cl}} - \frac{4m_{\text{He}}^2}{\beta \hbar^2} \langle A_\alpha^2 \rangle, \quad (\text{C4})$$

with I_α^{cl} the α principal component of the classical moment of inertia, which can be expressed as

$$I_\alpha^{\text{cl}} = \left\langle \frac{m_{\text{He}}}{P} \sum_{i=1}^{N_{\text{He}}} \sum_{s=1}^P (\vec{e}_\alpha \times \vec{r}_{i,s}) \cdot (\vec{e}_\alpha \times \vec{r}_{i,s+1}) \right\rangle, \quad (\text{C5})$$

and A_α^2 the square of the vectorial area of the Feynman paths,

$$\vec{A} = \frac{1}{2} \sum_{i=1}^{N_{\text{He}}} \sum_{s=1}^P \vec{r}_{i,s} \times \vec{r}_{i,s+1}, \quad (\text{C6})$$

i.e., the area spanned by the ring polymer, projected along the \vec{e}_α direction. The second term on the right-hand side of Eq. (C4) quantifies the quantum reduction of the effective moment of inertia due to superfluidity. The superfluid fraction is thus obtained in a similar way as in Eq. (C2):

$$f_s^\alpha = 1 - \frac{I_\alpha^{\text{eff}}}{I_\alpha^{\text{cl}}} = \frac{4m_{\text{He}}^2 \langle A_\alpha^2 \rangle}{\beta \hbar^2 I_\alpha^{\text{cl}}}. \quad (\text{C7})$$

This estimator is referred to as the area estimator and was introduced for the study of pure helium clusters [18]; a detailed discussion and derivation can be found in Ref. [77].

Obviously, superfluidity is a macroscopic phenomenon and the concept is not well defined for finite size systems. Nevertheless, it has been demonstrated that clusters of pure helium as small as 64 ^4He atoms exhibits clear manifestations of superfluid behavior [18]. Moreover, the study of rotational constants of various molecules as a function of the number n of helium atoms has revealed the onset of superfluid behavior for doped clusters composed of less than 10 ^4He atoms, leading to many studies on the concept of microscopic molecular superfluid response [27,29,33,77].

It is important to note that the area estimator, which has been devised for sufficiently large clusters, will necessarily overestimate the superfluid fraction for small clusters, since also non-exchanging paths span a finite area. In particular, in the limit of only one helium atom, Eq. (C7) leads to an unphysical finite superfluid fraction and for small clusters it can result in f_s values that are systematically too large and even greater than unity. The estimator is formally only valid in the thermodynamic limit for which the long exchange paths completely dominate the contributions due to the smaller nonexchanging paths. Thus, Eq. (C7) should be used with great caution for very small clusters. To circumvent this problem, a rescaled estimator that aims at removing the contribution of nonexchanging paths from the area estimator has recently been introduced [77,78]. This so-called exchange estimator is defined as

$$f_s^\alpha = \frac{I_{\alpha,\text{MB}}^{\text{eff}} - I_{\alpha,\text{BE}}^{\text{eff}}}{I_{\alpha,\text{MB}}^{\text{eff}}} = 1 - \frac{I_{\alpha,\text{BE}}^{\text{eff}}}{I_{\alpha,\text{MB}}^{\text{eff}}}, \quad (\text{C8})$$

with $I_{\text{MB}}^{\text{eff}}$ the effective moment of inertia, obtained from a path integral simulation in which the helium follows Maxwell-Boltzmann statistics (i.e., without quantum exchange and thus neglecting the bosonic nature of ^4He) and $I_{\text{BE}}^{\text{eff}}$ is the effective moment of inertia obtained from a bosonic treatment of the helium. This estimator is able to isolate the contribution to the area coming only from the exchanging paths and has thus been dubbed the exchange (X) estimator.

Figure 17 shows the superfluid fraction obtained using the standard area estimator as a function of the number of helium atoms computed in the space fixed frame (or laboratory frame). The first observation is the striking difference between the superfluid fractions obtained around a fully flexible and a completely fixed CH_5^+ , discussed in detail in the main text

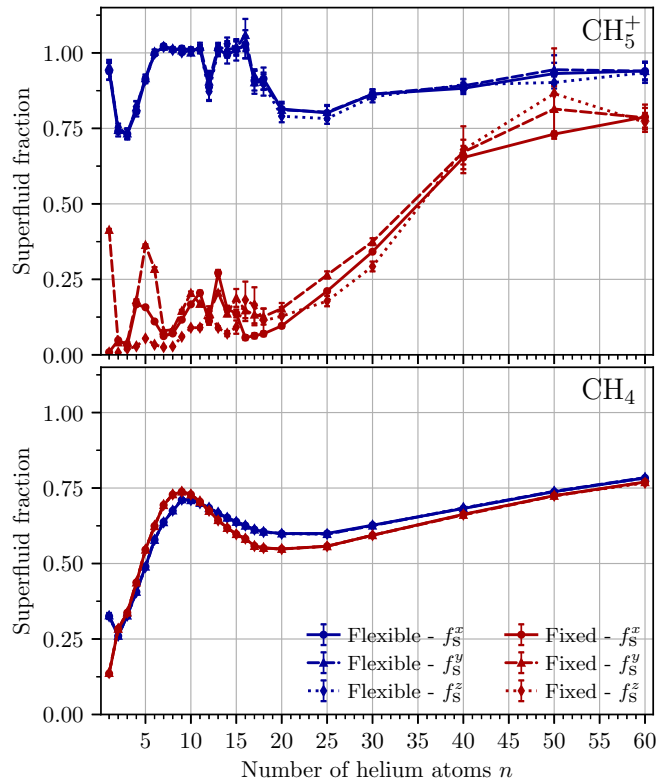


FIG. 17. Superfluid fraction along the x, y and z direction at $T = 0.5$ K as a function of the number of helium atoms around CH_5^+ (top) and CH_4 (bottom) computed using the area estimator [Eq. (C7)]. The red lines correspond to the results obtained with a molecule completely fixed in its minimum energy configuration, while the blue lines show the results obtained with a fully flexible impurity.

of the paper. Neglecting the molecular degrees of freedom of CH_5^+ results in a significant suppression of the superfluid fraction. As discussed in detail in the main text, this effect directly comes from the high degree of localization of ^4He in the first shell that hinders the creation of long exchange cycles and thus suppresses superfluidity in the first shell. Upon increasing the size of the cluster, the difference between the flexible and fixed case is considerably reduced—but only since the relative impact of what happens in the first shell on the total superfluid fraction of the entire cluster decreases for large n values. The effect remains, however, present in the first shell as can be seen from the local superfluid density (Figs. 20 and 4 of the main text) for $\text{CH}_5^+ \cdot \text{He}_{60}$. In the case of CH_4 , this impact of the molecular degrees of freedom is not found and the values of f_s obtained with a flexible or fixed impurity are very similar. It is interesting to note as well that around the fixed CH_5^+ molecule, the obtained superfluid fraction is not isotropic due to the pronounced asymmetry of the $\text{CH}_5^+ \cdots \text{He}$ potential, thus yielding different values f_s^α for the three different directions α . This effect is not present in the flexible case due to molecular rotations and is also not seen around the fixed CH_4 molecule due to the high symmetry of the $\text{CH}_4 \cdots \text{He}$ potential.

For very small numbers of helium atoms, significant superfluid fractions are obtained around the flexible CH_5^+ and, in

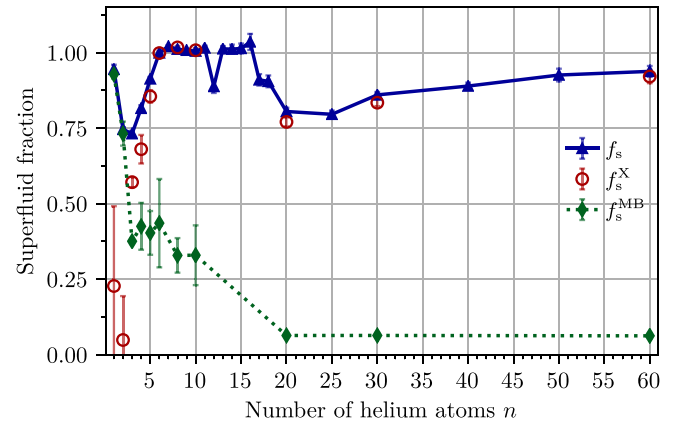


FIG. 18. Superfluid fraction f_s computed using the area estimator [Eq. (C7)] and f_s^X computed using the exchange estimator [Eq. (C8)] as a function of the number of helium atoms around flexible CH_5^+ at $T = 0.5$ K. The superfluid fraction is computed as an average over the three directions since f_s is isotropic here. Additionally, the superfluid fraction formally computed using the area estimator applied to nonbosonic Maxwell-Boltzmann simulations, f_s^{MB} , is included as well to give an estimation of the contribution of the nonexchanging paths to f_s obtained from the area estimator.

particular, a finite superfluid fraction is observed with a single helium atom, which is a clear illustration of the failure of the area estimator for very small clusters as is well-known from the literature. Upon increasing the number of helium atoms n for CH_5^+ , the superfluid fraction quickly reaches unity for $6 < n < 16$ except for the special case of 12 ^4He atoms, discussed in detail in the following. For $n > 16$, the total superfluid fraction in the entire cluster drops due to the creation of the second helium solvation shell, which features a smaller density that prevents the creation of long exchange paths. Upon building this second solvation shell, the associated density increases again for $n \gg 16$ and so does the superfluid fraction reaching around 0.9 for the largest cluster of 60 ^4He atoms. In the case of CH_4 , the superfluid fraction reaches a first maximum for $n = 9$, which also corresponds to the beginning of the building of a second solvation shell (see Fig. 16), in which the density and thus the superfluid fraction is lower. Upon building this second solvation shell, the superfluid fraction increases again to reach a value of around 0.75 for the largest cluster of 60 ^4He atoms.

To estimate the validity of the superfluid fractions computed here using the area estimator, we have performed additional simulations without bosonic exchange for a few selected numbers of helium atoms around flexible protonated methane to compute the superfluid fraction using the exchange estimator [77,78] of Eq. (C8). The comparison between the superfluid fraction obtained using the two estimators is presented in Fig. 18. It is clear that except for very small numbers of helium atoms, the area estimator provides a very good estimation of the superfluid fraction, since both estimators provide almost the same value for $n > 5$ ^4He atoms (thus, the blue triangles and red circles are close to each other). Only in the small cluster limit (in particular for ≤ 4), the exchange estimator (red circles) yields substantially smaller f_s

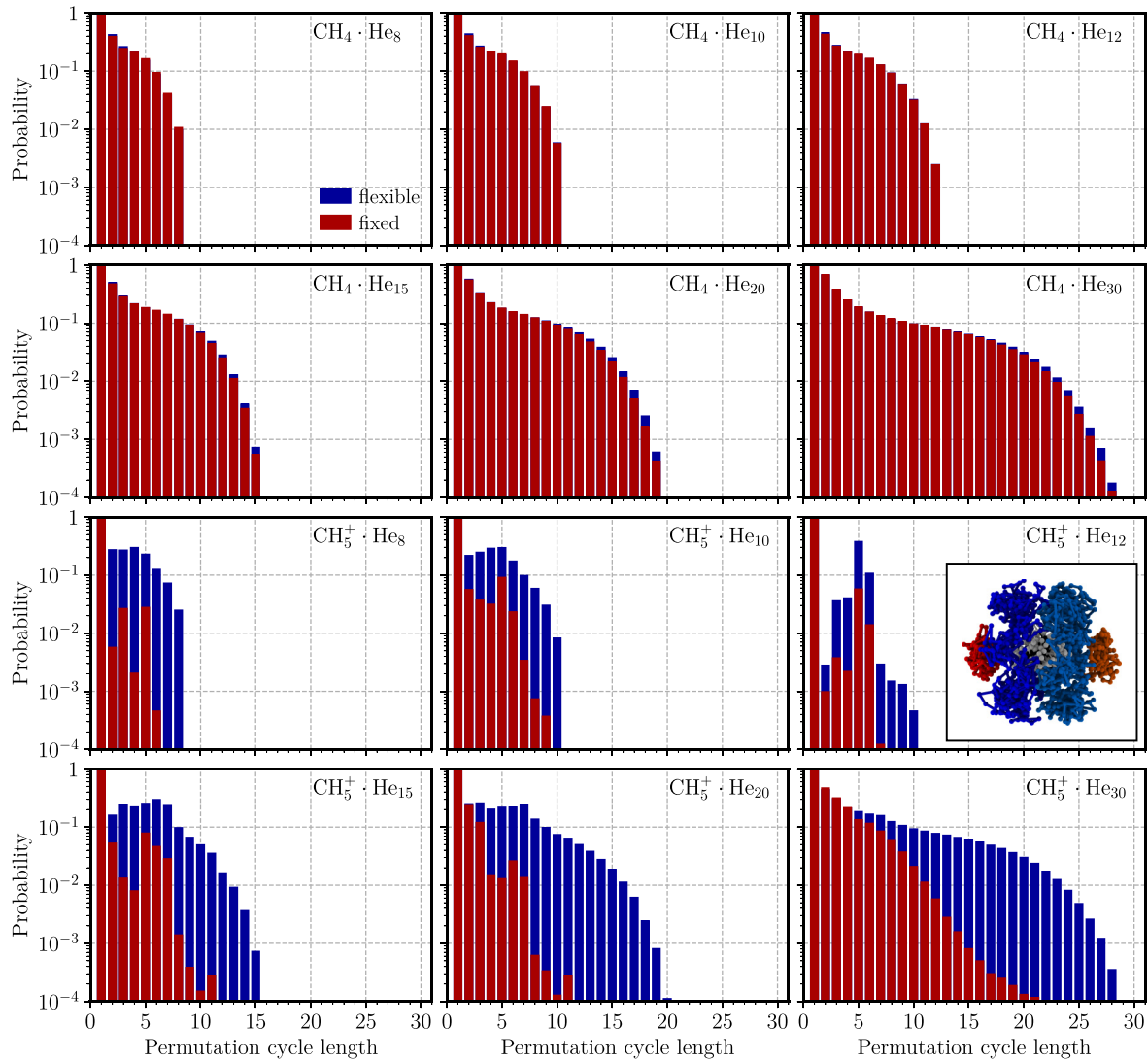


FIG. 19. Probability of finding at least one exchange path of specific length for $\text{CH}_4 \cdot {}^4\text{He}_n$ (first two rows) and $\text{CH}_5^+ \cdot {}^4\text{He}_n$ (second two rows) at $T = 0.5$ K for different clusters sizes n as indicated. Data for the flexible and fixed impurities are shown in blue and red, respectively; note that blue is superimposed by red where not visible. The inset of $\text{CH}_5^+ \cdot {}^4\text{He}_{12}$ depicts a representative snapshot from the simulation, illustrating a typical arrangement of the helium atoms for this very special case, see text. The helium beads represented with the same color belongs to the same exchange cycle.

values and eventually approaches the expected limit, namely, zero, within error bars. It is well-known that superfluidity is directly connected to the presence of long exchange cycles [30,50,57], i.e., of path lengths comparable to the system size, and the statistics of exchange path length, as shown in Fig. 19, can thus provide complementary insight into the origin of the superfluid response. The exchange path statistics clearly confirm that, in the case of CH_4 , the molecular degrees of freedom have no significant impact on bosonic exchange and thus on the superfluid behavior of helium. In the case of CH_5^+ however, there is a clear coupling between the molecular motion and bosonic exchange and, in particular, neglecting the molecular degrees of freedom by fixing CH_5^+ in space tends to significantly reduce the probability of building long exchange cycles, which reduces the superfluid response.

A special case appears for $\text{CH}_5^+ \cdot \text{He}_{12}$, for which a sudden drop of the superfluid fraction is also noticed in Fig. 17. This effect is related to a particularly stable configuration of the helium atoms, forming two parallel rings of five atoms around CH_5^+ , with the last two atoms being located at two opposite ends of the molecule, as shown in the inset of $\text{CH}_5^+ \cdot {}^4\text{He}_{12}$ in Fig. 19. This configuration in Cartesian space leads to a special distribution in permutation space as well, with the exchange path length of five being overrepresented, as such rings are mostly found in exchange cycles involving all five atoms. Similar configurations have been previously observed for instance in para- H_2 clusters doped with a water molecule [79], thus indicating that this specific topology of the exchange path might be a universal feature of doped bosonic clusters featuring a strong molecule-solvent interaction.

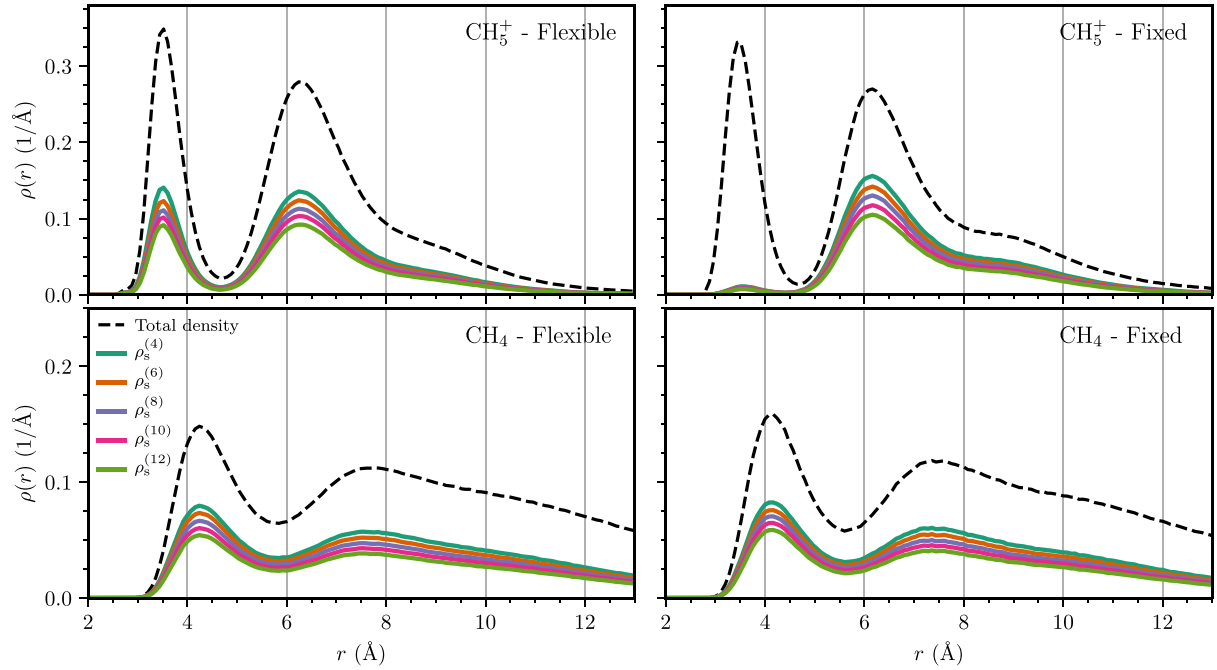


FIG. 20. Local superfluid density $\rho_s^{(l)}$ for $\text{CH}_5^+ \cdot \text{He}_{60}$ (first row) $\text{CH}_4 \cdot \text{He}_{60}$ (second row) computed using the local exchange path estimator of Eq. (C9) at $T = 0.5$ K using different values of the cutoff length l , where r is the distance between the carbon nucleus with respect to helium, see text. Left and right columns are for flexible and fixed molecules, respectively.

2. Local superfluid density

The well-known connection between the presence of long exchange paths and superfluidity [30,50,57] can actually be used as a proxy to obtain local information on the superfluid behavior of the helium solvent. In particular, an estimator of the local superfluid density $\rho_s(r)$ was introduced [30] based on the distributions of helium atoms involved in an exchange path longer than a certain cutoff length l ,

$$\rho_s^{(l)}(\vec{r}) = \sum_{p>l}^{N_{\text{He}}} \rho_p(\vec{r}), \quad (\text{C9})$$

where $\rho_p(\vec{r})$ is the local density of helium involved in an exchange cycle of length p at point \vec{r} in space. Figure 20 displays the local superfluid density obtained using this local exchange path estimator for different l parameters, where r is the distance between the carbon nucleus in CH_5^+ and CH_4 with respect to helium. In particular, the impact of the choice of the cutoff to distinguish between short and long exchange paths is investigated in the following. While the obtained superfluid densities clearly depend on the value of the cutoff parameter l , their shapes remain unchanged for different values of l and Eq. (C9) thus provides a relatively robust estimator of the superfluid density. The results presented in the main text are obtained using a cutoff of $l = 6$. However, the estimator tends to systematically underestimate the superfluid density, as expected based on its definition. Short paths and, in particular, nonexchanging ones, strongly contribute to the normal density in this estimator, even though such paths are also present in a fully superfluid case. Nevertheless, this estimator of the local superfluid density still grants access to a well-defined locally resolved estimation of the superfluid response, as we

will demonstrate in what follows by comparing the results provided by this estimator (as discussed in the main text) with those using another local estimator.

An alternative local estimator based on the area of the Feynman paths in a similar way as the (global) area estimator of the superfluid fraction has also been developed [31,80]. In particular, a local area estimator of the superfluid density has been introduced, which leads to the correct value of the effective moment of inertia [80]:

$$I_\alpha^{\text{eff}} = \int (\rho(\vec{r}) - \rho_s^\alpha(\vec{r})) r_\perp^2 d^3\vec{r}, \quad (\text{C10})$$

$$I_\alpha^{\text{eff}} = I_\alpha^{\text{cl}} - \int \rho_s^\alpha(\vec{r}) r_\perp^2 d^3\vec{r}. \quad (\text{C11})$$

The last term on the right-hand side clearly represents the quantum reduction of the effective moment of inertia due to superfluidity and is given by

$$\int \rho_s^\alpha(\vec{r}) r_\perp^2 d^3\vec{r} = \frac{4m_{\text{He}}^2}{\beta\hbar^2} \langle A_\alpha^2 \rangle, \quad (\text{C12})$$

from which the following superfluid density estimator can be obtained [80]:

$$\rho_s^\alpha(\vec{r}) = \frac{4m_{\text{He}}^2 \langle A_\alpha A_\alpha(\vec{r}) \rangle}{\beta\hbar^2 r_\perp^2}, \quad (\text{C13})$$

with $A_\alpha(\vec{r})$ the local contribution to the area defined as

$$A_\alpha(\vec{r}) = \frac{1}{2} \sum_{i=1}^{N_{\text{He}}} \sum_{s=1}^P (\vec{r}_{i,s} \times \vec{r}_{i,s+1})_\alpha \delta(\vec{r}_{i,s} - \vec{r}). \quad (\text{C14})$$

A local superfluid fraction can then be defined as well,

$$\frac{\rho_s^\alpha(\vec{r})}{\rho(\vec{r})} = \frac{4m_{\text{He}}^2 \langle A_\alpha A_\alpha(\vec{r}) \rangle}{\beta \hbar^2 I^{\text{cl}}(\vec{r})}, \quad (\text{C15})$$

which can be used to compute the values of the superfluid fraction associated with different regions, such as the first and second shells, by locally averaging the contribution to the local exchange area and moment of inertia [80]. This can furthermore be used to define a radial superfluid fraction or, equivalently, a radial superfluid density,

$$\rho_s^\alpha(r) = \frac{4m_{\text{He}}^2 \langle A_\alpha A_\alpha(r) \rangle}{\beta \hbar^2 I^{\text{cl}}(r)} \rho(r), \quad (\text{C16})$$

as shown in the bottom panel of Fig. 4 of the main text. Note that the distance r corresponds here to the distance of helium with respect to the center of mass of the molecule computed using all the beads (rather than to the C atom of the respective molecule as used in Fig. 20). The differences between the total helium density in Fig. 4 of the main text are simply due to this change of the reference point for computing distances, noting that the center of mass distance is a more natural choice for the local area estimator. Indeed, the vectorial product in Eq. (C14) requires a common origin for the two position vectors, which should thus not depend on the bead index and we chose here to use the molecular center of mass computed using all the beads.

As mentioned in the main text, both estimators provide the same overall picture for both impurities, in particular, the distance modulations of the superfluid response within the first and second helium shells when comparing the flexible to the fixed impurity scenario. Yet, despite providing such qualitative agreement, the local area estimator leads to superfluid densities that are typically quantitatively different in numbers from the ones obtained using the local exchange path estimator (see Fig. 20). In particular, with this estimator, we find that the global superfluid fraction associated with the $\text{CH}_4 \cdot \text{He}_{60}$ complex is 0.86, which is larger in number than the value of 0.78 obtained using the associated global superfluid fraction estimator of Eq. (C7). In the case of the $\text{CH}_5^+ \cdot \text{He}_{60}$ complex, the obtained superfluid density indicates that the cluster is essentially fully superfluid around flexible CH_5^+ with an associated global superfluid fraction of 0.96, which is indeed very similar to the value of 0.94 that we obtained using the global estimator of Eq. (C7). In particular, the first solvation shell is fully superfluid. In the case of the fixed protonated methane, the obtained superfluid density indicates, as expected, a much lower superfluid fraction estimated to be around 0.68, which is even smaller than the value of 0.78 obtained with the global estimator. The superfluid density in the first shell is particularly impacted and the associated superfluid fraction dropped to 0.28 as a result of the strong localization of helium as discussed in the main text.

In summary, both estimators fully consistently disclose that sufficiently large $\text{CH}_5^+ \cdot \text{He}_n$ complexes feature a strong superfluid response of the first (frozen) solvation shell in the fully flexible case, and thus manifestations of supersolid behavior, which is lost if the large-amplitude rovibrational degrees of freedom of the molecule are neglected by fixing all intramolecular molecular degrees of freedom, as discussed in

detail in the main text. Recall that this phenomenon, which can only be observed with sufficiently many helium atoms to fully solvate the molecular impurity, thus filling the first solvation shell, cannot appear in the microsolvation limit and is thus strikingly different from what has been discovered earlier [47] for very small $\text{CH}_5^+ \cdot \text{He}_n$ up to $n = 4$.

APPENDIX D: MICROSOLVATION LIMIT

The microsolvation of CH_5^+ up to a maximum number of four helium atoms has been studied [47,58], which we discuss in the following in relation to our current paper that focuses on unique effects of this impurity seen in the realm of large ^4He clusters. Previously, an intricate coupling between the molecular motion of the impurity and bosonic exchange of helium has been discovered for such tiny $\text{CH}_5^+ \cdot ^4\text{He}_n$ clusters with n up to four helium atoms [47]. Such small system sizes n are of particular interest to ^4He -based tagging spectroscopy [81–83]. Given the lack of a well-defined, unique estimator to compute the superfluid fraction in the limit of a small number of ^4He atoms (as discussed here in Sec. C 1), which is particularly relevant for $\text{CH}_5^+ \cdot ^4\text{He}_n$ with $n \leq 4$, the previous analysis [47] has been performed entirely at the qualitative level. In particular, the exchange path statistics of those paths that include all available n ^4He atoms, i.e., as few as $n = 2, 3$, and 4 in this case, has been studied; this approach closely follows pioneering work [30,57] on using “sufficiently long” exchange cycles as a proxy to detect superfluid behavior.

Here, in stark contrast, we are interested in the opposite limit to microsolvation, namely, completely filling the first solvation shell and going beyond by studying large clusters with up to $n = 60$ ^4He atoms that solvate the CH_5^+ molecule. We demonstrate, based on Fig. 18, that the area and exchange estimators reviewed in Appendix C 1 provide very similar superfluid fractions only for $n \geq 6$ which remains so all the way up to the largest cluster $n = 60$. We therefore refrain here from discussing the superfluid fraction for $\text{CH}_5^+ \cdot ^4\text{He}_n$ clusters with $n < 6$ given the strongly different f_s results and, thus, ambiguity in the microsolvation limit. Moreover, we study here only either the fully flexible or the frozen CH_5^+ core within the $\text{CH}_5^+ \cdot ^4\text{He}_n$ clusters, whereas major insights on the impact of large-amplitude motion on bosonic exchange within microsolvated clusters with $n \leq 4$ were enabled in the previous study [47] by performing so-called e- C_s restrained simulations to generate data on a useful reference system (namely, the one that allows only for small-amplitude motion while not being fixed in space). This aspect is not at all in the focus of the present investigation on $\text{CH}_5^+ \cdot ^4\text{He}_n$ clusters that is devoted to what happens in the limit of large clusters, in particular, beyond having filled the first solvation shell. For this purpose, we introduce $\text{CH}_4 \cdot ^4\text{He}_n$ clusters to provide the proper reference system to assess effects due to large-amplitude motion (which only operate in CH_5^+) since CH_4 is a standard quasirigid molecule subject to small-amplitude motion that is well described by quasiharmonic deviations from a unique equilibrium structure.

Apart from that, we achieved major improvements of the accuracy of the interactions, i.e., the CH_5^+ potential energy surface and the $\text{CH}_5^+ \cdots ^4\text{He}$ interaction potential that we can now use compared to previously [47]. In that work, a

simple force field description of the CH_5^+ potential energy surface has been used, the so-called POSflex model [84], where all five C–H bond distances have the same equilibrium length, thus all protons move on a sphere centered around the carbon site. This force field is computationally highly efficient, but only allows for a merely qualitatively satisfactory description of the properties of CH_5^+ as demonstrated previously [84], since POSflex does not take into account the characteristically different lengths [44] of the three-center versus two-center C–H bonds within CH_5^+ . Second, the potential constructed previously to describe the $\text{CH}_5^+ \cdots {}^4\text{He}$ interactions is based on a complicated, traditional force fieldlike representation fitted against coupled cluster interaction energies [85]. Unfortunately, this potential is only able to provide a satisfactory description of very small $\text{CH}_5^+ \cdots {}^4\text{He}_n$ clusters up to only four ${}^4\text{He}$ atoms [85], whereas it has been found to fail even qualitatively for $n > 4$. Thus, the present paper would not have been possible using this existing interaction potential.

In the current paper, in stark contrast to our previous investigation [47], we greatly improved the quality of all interactions, both intra- and intermolecular, and pushed them to the converged coupled cluster level, CCSD(T), enabled by using our high-dimensional neural network potential approach for finite systems [55,56] at what is often called chemical accuracy. This major development is comprehensively presented in a self-contained manner in Appendix A where we

describe in detail the generation and validation of the CH_5^+ and CH_4 potential energy surfaces as well as the $\text{CH}_5^+ \cdots {}^4\text{He}$ and $\text{CH}_4 \cdots {}^4\text{He}$ interaction potentials that we introduced and used in the present investigation for the first time.

Another significant improvement of the present paper versus our previous work [47] is related to the colored-noise thermostating scheme within the path integral approach to effectively enhance the convergence of the Trotter decomposition. The currently used PIQTB technique [53], carefully validated for use at very low temperatures [54], allows us to reach a temperature of 0.5 K in a PIMD setup, whereas previously, using the PIGLET technique [86,87], we were able to reach only 1.25 K, where bosonic exchange effects are, of course, much less pronounced.

Overall, our present quantum simulation approach significantly transcends, both in accuracy and convergence, the one used a few years back [47] to study microsolvated $\text{CH}_5^+ \cdots {}^4\text{He}_n$ clusters with $n \leq 4$ in many ways. Only these significant improvements grant access to accurately simulating large $\text{CH}_5^+ \cdots {}^4\text{He}_n$ clusters—which provides the basis to discover a unique effect, namely, *manifestations of supersolid behavior*. We refer the interested reader to a recent review where all these major improvements of our neural network-based bosonic path integral simulation methodology, which enables converged quantum simulations of complex molecular systems such as the present one at very low temperatures, are explained and validated in detail [48].

-
- [1] A. J. Leggett, Can a solid be “superfluid”? *Phys. Rev. Lett.* **25**, 1543 (1970).
- [2] M. Boninsegni and N. V. Prokofev, *Colloquium: Supersolids: What and where are they?* *Rev. Mod. Phys.* **84**, 759 (2012).
- [3] A. F. Andreev and I. M. Lifshitz, Quantum theory of defects in crystals, *Zh. Eksp. Teor. Fiz.* **56**, 2057 (1969) [*Sov. Phys. JETP* **29**, 1107 (1969)].
- [4] L. Reatto, Bose-Einstein condensation for a class of wave functions, *Phys. Rev.* **183**, 334 (1969).
- [5] J.-R. Li, J. Lee, W. Huang, S. Burchesky, B. Shteynas, F. C. Top, A. O. Jamison, and W. Ketterle, A stripe phase with supersolid properties in spin-orbit-coupled Bose-Einstein condensates, *Nature (London)* **543**, 91 (2017).
- [6] M. A. Norcia, C. Politi, L. Klaus, E. Poli, M. Sohmen, M. J. Mark, R. N. Bisset, L. Santos, and F. Ferlaino, Two-dimensional supersolidity in a dipolar quantum gas, *Nature (London)* **596**, 357 (2021).
- [7] T. Bland, E. Poli, C. Politi, L. Klaus, M. A. Norcia, F. Ferlaino, L. Santos, and R. N. Bisset, Two-dimensional supersolid formation in dipolar condensates, *Phys. Rev. Lett.* **128**, 195302 (2022).
- [8] C. W. Myung, B. Hirshberg, and M. Parrinello, Prediction of a supersolid phase in high-pressure deuterium, *Phys. Rev. Lett.* **128**, 045301 (2022).
- [9] P. Sindzingre, D. M. Ceperley, and M. L. Klein, Superfluidity in clusters of *p*- H_2 molecules, *Phys. Rev. Lett.* **67**, 1871 (1991).
- [10] F. Mezzacapo and M. Boninsegni, On the possible supersolid character of parahydrogen clusters, *J. Phys. Chem. A* **115**, 6831 (2011).
- [11] E. Kim and M. H. W. Chan, Probable observation of a supersolid helium phase, *Nature (London)* **427**, 225 (2004).
- [12] S. Balibar, The enigma of supersolidity, *Nature (London)* **464**, 176 (2010).
- [13] D. Y. Kim and M. H. W. Chan, Absence of supersolidity in solid helium in porous Vycor glass, *Phys. Rev. Lett.* **109**, 155301 (2012).
- [14] J. Choi, A. A. Zadorozhko, J. Choi, and E. Kim, Spatially modulated superfluid state in two-dimensional ${}^4\text{He}$ films, *Phys. Rev. Lett.* **127**, 135301 (2021).
- [15] S. Grebenev, J. P. Toennies, and A. F. Vilesov, Superfluidity within a small helium-4 cluster: The microscopic Andronikashvili experiment, *Science* **279**, 2083 (1998).
- [16] J. P. Toennies and A. F. Vilesov, Spectroscopy of atoms and molecules in liquid helium, *Annu. Rev. Phys. Chem.* **49**, 1 (1998).
- [17] J. P. Toennies and A. F. Vilesov, Superfluid helium droplets: A uniquely cold nanomatrix for molecules and molecular complexes, *Angew. Chem. Int. Ed.* **43**, 2622 (2004).
- [18] P. Sindzingre, M. L. Klein, and D. M. Ceperley, Path-integral Monte Carlo study of low-temperature ${}^4\text{He}$ clusters, *Phys. Rev. Lett.* **63**, 1601 (1989).
- [19] K. R. Atkins, Ions in liquid helium, *Phys. Rev.* **116**, 1339 (1959).
- [20] A. Nakayama and K. Yamashita, Theoretical study on the structure of Na^+ -doped helium clusters: Path integral Monte Carlo calculations, *J. Chem. Phys.* **112**, 10966 (2000).

- [21] M. Buzzacchi, D. E. Galli, and L. Reatto, Alkali ions in superfluid ^4He and structure of the snowball, *Phys. Rev. B* **64**, 094512 (2001).
- [22] D. E. Galli, D. M. Ceperley, and L. Reatto, Path integral Monte Carlo of ^4He clusters doped with alkali and alkali-earth ions, *J. Phys. Chem. A* **115**, 7300 (2011).
- [23] J. Poitrenaud and F. I. B. Williams, Precise measurement of effective mass of positive and negative charge carriers in liquid helium II, *Phys. Rev. Lett.* **29**, 1230 (1972).
- [24] S. Müller, M. Mudrich, and F. Stienkemeier, Alkali-helium snowball complexes formed on helium nanodroplets, *J. Chem. Phys.* **131**, 044319 (2009).
- [25] P. Bartl, C. Leidlmair, S. Denifl, P. Scheier, and O. Echt, On the size and structure of helium snowballs formed around charged atoms and clusters of noble gases, *J. Phys. Chem. A* **118**, 8050 (2014).
- [26] F. J. Bartis, The mobility of positive ions with large He I halos, *Phys. Lett. A* **60**, 417 (1977).
- [27] J. Tang, Y. Xu, A. R. W. McKellar, and W. Jäger, Quantum solvation of carbonyl sulfide with helium atoms, *Science* **297**, 2030 (2002).
- [28] Y. Xu, W. Jäger, J. Tang, and A. R. W. McKellar, Spectroscopic studies of quantum solvation in $^4\text{He}_N\text{-N}_2\text{O}$ clusters, *Phys. Rev. Lett.* **91**, 163401 (2003).
- [29] A. R. W. McKellar, Y. Xu, and W. Jäger, Spectroscopic exploration of atomic scale superfluidity in doped helium nanoclusters, *Phys. Rev. Lett.* **97**, 183401 (2006).
- [30] Y. Kwon and K. B. Whaley, Atomic-scale quantum solvation structure in superfluid helium-4 clusters, *Phys. Rev. Lett.* **83**, 4108 (1999).
- [31] E. W. Draeger and D. M. Ceperley, Superfluidity in a doped helium droplet, *Phys. Rev. Lett.* **90**, 065301 (2003).
- [32] S. Moroni, A. Sarsa, S. Fantoni, K. E. Schmidt, and S. Baroni, Structure, Rotational dynamics, and superfluidity of small OCS-doped He clusters, *Phys. Rev. Lett.* **90**, 143401 (2003).
- [33] J. Tang, A. R. W. McKellar, F. Mezzacapo, and S. Moroni, Bridging the gap between small clusters and nanodroplets: Spectroscopic study and computer simulation of carbon dioxide solvated with helium atoms, *Phys. Rev. Lett.* **92**, 145503 (2004).
- [34] F. Paesani, Y. Kwon, and K. B. Whaley, Onset of superfluidity in small $\text{CO}_2(^4\text{He})_N$ clusters, *Phys. Rev. Lett.* **94**, 153401 (2005).
- [35] C. C. Duminuco, D. E. Galli, and L. Reatto, Local solid order around impurities: Doped clusters and ions in ^4He , *Phys. B: Condens. Matter* **284-288**, 109 (2000).
- [36] Y. Kwon, P. Huang, M. V. Patel, D. Blume, and K. B. Whaley, Quantum solvation and molecular rotations in superfluid helium clusters, *J. Chem. Phys.* **113**, 6469 (2000).
- [37] N. Blinov, X. Song, and P.-N. Roy, Path integral Monte Carlo approach for weakly bound van der Waals complexes with rotations: Algorithm and benchmark calculations, *J. Chem. Phys.* **120**, 5916 (2004).
- [38] R. E. Zillich, F. Paesani, Y. Kwon, and K. B. Whaley, Path integral methods for rotating molecules in superfluids, *J. Chem. Phys.* **123**, 114301 (2005).
- [39] N. D. Markovskiy and C. H. Mak, Path integral studies of the rotations of methane and its heavier isotopomers in ^4He nanoclusters, *J. Phys. Chem. A* **113**, 9165 (2009).
- [40] Y. Kwon and H. Shin, Superfluidity and structural order in ^4He adsorbed on a C_{20} molecule: Path-integral Monte Carlo calculations, *Phys. Rev. B* **82**, 172506 (2010).
- [41] P. A. Crowell and J. D. Reppy, Superfluidity and film structure in ^4He adsorbed on graphite, *Phys. Rev. B* **53**, 2701 (1996).
- [42] J. Nyéki, A. Phillis, B. Cowan, and J. Saunders, On the super-solid response of the second layer of ^4He on graphite, *J. Low Temp. Phys.* **187**, 475 (2017).
- [43] J. Nyéki, A. Phillis, A. Ho, D. Lee, P. Coleman, J. Parpia, B. Cowan, and J. Saunders, Intertwined superfluid and density wave order in two-dimensional ^4He , *Nat. Phys.* **13**, 455 (2017).
- [44] D. Marx and M. Parrinello, Structural quantum effects and three-centre two-electron bonding in CH_5^+ , *Nature (London)* **375**, 216 (1995).
- [45] H. Schmiedt, P. Jensen, and S. Schlemmer, Collective molecular superrotation: A model for extremely flexible molecules applied to protonated methane, *Phys. Rev. Lett.* **117**, 223002 (2016).
- [46] J. Davies, S. Yang, and A. M. Ellis, Infrared spectra of carbocations and CH_4^+ in helium, *Phys. Chem. Chem. Phys.* **23**, 27449 (2021).
- [47] F. Uhl and D. Marx, Quantum microsolvation of protonated methane with ^4He : Large-amplitude motion heavily influences bosonic exchange, *Phys. Rev. Lett.* **123**, 123002 (2019).
- [48] F. Brieuc, C. Schran, F. Uhl, H. Forbert, and D. Marx, Converged quantum simulations of reactive solutes in superfluid helium: The Bochum perspective, *J. Chem. Phys.* **152**, 210901 (2020).
- [49] L. Walewski, H. Forbert, and D. Marx, Reactive path integral quantum simulations of molecules solvated in superfluid helium, *Comput. Phys. Commun.* **185**, 884 (2014).
- [50] D. M. Ceperley, Path integrals in the theory of condensed helium, *Rev. Mod. Phys.* **67**, 279 (1995).
- [51] M. Boninsegni, N. Prokof'ev, and B. Svistunov, Worm algorithm for continuous-space path integral Monte Carlo simulations, *Phys. Rev. Lett.* **96**, 070601 (2006).
- [52] M. Boninsegni, N. V. Prokof'ev, and B. V. Svistunov, Worm algorithm and diagrammatic Monte Carlo: A new approach to continuous-space path integral Monte Carlo simulations, *Phys. Rev. E* **74**, 036701 (2006).
- [53] F. Brieuc, H. Dammak, and M. Hayoun, Quantum thermal bath for path integral molecular dynamics simulation, *J. Chem. Theory Comput.* **12**, 1351 (2016).
- [54] C. Schran, F. Brieuc, and D. Marx, Converged colored noise path integral molecular dynamics study of the Zundel cation down to ultralow temperatures at coupled cluster accuracy, *J. Chem. Theory Comput.* **14**, 5068 (2018).
- [55] C. Schran, F. Uhl, J. Behler, and D. Marx, High-dimensional neural network potentials for solvation: The case of protonated water clusters in helium, *J. Chem. Phys.* **148**, 102310 (2017).
- [56] C. Schran, J. Behler, and D. Marx, Automated fitting of neural network potentials at coupled cluster accuracy: Protonated water clusters as testing ground, *J. Chem. Theory Comput.* **16**, 88 (2020).
- [57] W. Krauth, Quantum Monte Carlo calculations for a large number of bosons in a harmonic trap, *Phys. Rev. Lett.* **77**, 3695 (1996).
- [58] F. Uhl and D. Marx, Helium tagging of protonated methane in messenger spectroscopy: Does it interfere with the fluxionality of CH_5^+ ? *Angew. Chem. Int. Ed.* **57**, 14792 (2018).
- [59] See Supplemental Material at <http://link.aps.org/supplemental/10.1103/PhysRevResearch.5.043083> for a list of the parameters used to define all the NNPs.

- [60] J. A. Davies, N. A. Besley, S. Yang, and A. M. Ellis, Probing elusive cations: Infrared spectroscopy of protonated acetic acid, *J. Phys. Chem. Lett.* **10**, 2108 (2019).
- [61] S. Erukala, D. Verma, and A. Vilesov, Rotation of CH_3^+ cations in helium droplets, *J. Phys. Chem. Lett.* **12**, 5105 (2021).
- [62] J. A. Davies, C. Schran, F. Briec, D. Marx, and A. M. Ellis, Onset of rotational decoupling for a molecular ion solvated in helium: From tags to rings and shells, *Phys. Rev. Lett.* **130**, 083001 (2023).
- [63] O. Asvany, P. Padma Kumar, B. Redlich, I. Hegemann, S. Schlemmer, and D. Marx, Understanding the infrared spectrum of bare CH_5^+ , *Science* **309**, 1219 (2005).
- [64] J. Behler and M. Parrinello, Generalized neural-network representation of high-dimensional potential-energy surfaces, *Phys. Rev. Lett.* **98**, 146401 (2007).
- [65] J. Behler, First principles neural network potentials for reactive simulations of large molecular and condensed systems, *Angew. Chem. Int. Ed.* **56**, 12828 (2017).
- [66] R. A. Kendall, T. H. Dunning, and R. J. Harrison, Electron affinities of the first-row atoms revisited. Systematic basis sets and wave functions, *J. Chem. Phys.* **96**, 6796 (1992).
- [67] D. E. Woon and T. H. Dunning, Gaussian basis sets for use in correlated molecular calculations. IV. Calculation of static electrical response properties, *J. Chem. Phys.* **100**, 2975 (1994).
- [68] T. B. Adler, G. Knizia, and H.-J. Werner, A simple and efficient CCSD(T)-F12 approximation, *J. Chem. Phys.* **127**, 221106 (2007).
- [69] G. Knizia, T. B. Adler, and H.-J. Werner, Simplified CCSD(T)-F12 methods: Theory and benchmarks, *J. Chem. Phys.* **130**, 054104 (2009).
- [70] H.-J. Werner, P. J. Knowles, G. Knizia, F. R. Manby, and M. Schütz, Molpro: A general-purpose quantum chemistry program package, *WIREs Comput Mol Sci* **2**, 242 (2012).
- [71] J. Behler, RuNNer: A program for constructing high-dimensional neural network potentials; Georg-August-Universität Göttingen, Germany, <https://www.uni-goettingen.de/de/560580.html>.
- [72] M. Gastegger and P. Marquetand, High-dimensional neural network potentials for organic reactions and an improved training algorithm, *J. Chem. Theory Comput.* **11**, 2187 (2015).
- [73] J. Behler, Atom-centered symmetry functions for constructing high-dimensional neural network potentials, *J. Chem. Phys.* **134**, 074106 (2011).
- [74] S. F. Boys and F. Bernardi, The calculation of small molecular interactions by the differences of separate total energies. Some procedures with reduced errors, *Mol. Phys.* **19**, 553 (1970).
- [75] O. Marchetti and H.-J. Werner, Accurate calculations of intermolecular interaction energies using explicitly correlated coupled cluster wave functions and a dispersion-weighted MP2 method, *J. Phys. Chem. A* **113**, 11580 (2009).
- [76] E. L. Andronikashvili, A direct observation of two kinds of motion in helium II, *J. Phys. USSR* **10**, 201 (1946).
- [77] T. Zeng and P.-N. Roy, Microscopic molecular superfluid response: Theory and simulations, *Rep. Prog. Phys.* **77**, 046601 (2014).
- [78] T. Zeng, G. Guillon, J. T. Cantin, and P.-N. Roy, Probing the superfluid response of para-hydrogen with a sulfur dioxide dopant, *J. Phys. Chem. Lett.* **4**, 2391 (2013).
- [79] T. Zeng, H. Li, and P.-N. Roy, Simulating asymmetric top impurities in superfluid clusters: A para-water dopant in para-hydrogen, *J. Phys. Chem. Lett.* **4**, 18 (2013).
- [80] Y. Kwon, F. Paesani, and K. B. Whaley, Local superfluidity in inhomogeneous quantum fluids, *Phys. Rev. B* **74**, 174522 (2006).
- [81] J. Roithová, A. Gray, E. Andris, J. Jašík, and D. Gerlich, Helium tagging infrared photodissociation spectroscopy of reactive ions, *Acc. Chem. Res.* **49**, 223 (2016).
- [82] M. Töpfer, T. Salomon, H. Kohguchi, O. Dopfer, K. M. T. Yamada, S. Schlemmer, and O. Asvany, Double resonance rotational spectroscopy of weakly bound ionic complexes: The case of floppy CH_3^+-He , *Phys. Rev. Lett.* **121**, 143001 (2018).
- [83] O. Asvany, S. Schlemmer, T. Szidarovszky, and A. G. Császár, Infrared signatures of the HHe_n^+ and DHe_n^+ ($n = 3-6$) complexes, *J. Phys. Chem. Lett.* **10**, 5325 (2019).
- [84] F. Uhl, L. Walewski, H. Forbert, and D. Marx, Adding flexibility to the particles-on-a-sphere model for large-amplitude motion: POSflex force field for protonated methane, *J. Chem. Phys.* **141**, 104110 (2014).
- [85] D. Kuchenbecker, F. Uhl, H. Forbert, G. Jansen, and D. Marx, Constructing accurate interaction potentials to describe the microsolvation of protonated methane by helium atoms, *Phys. Chem. Chem. Phys.* **19**, 8307 (2017).
- [86] M. Ceriotti and D. E. Manolopoulos, Efficient first-principles calculation of the quantum kinetic energy and momentum distribution of nuclei, *Phys. Rev. Lett.* **109**, 100604 (2012).
- [87] F. Uhl, D. Marx, and M. Ceriotti, Accelerated path integral methods for atomistic simulations at ultra-low temperatures, *J. Chem. Phys.* **145**, 054101 (2016).